



Mario Mühlbacher BSc.

PHYSICAL BASED FEATURE EXTRACTION FOR ACTIVE THERMOGRAPHY INSPECTION

MASTER'S THESIS

to achieve the university degree of

Diplom-Ingenieur

Master's degree programme: Information and Computer Engineering

submitted to

Graz University of Technology

Supervisor

Univ.-Prof. Dipl.-Ing. Dr.techn. Horst Bischof

Institute of Computer Graphics and Vision

Dipl.-Ing. Dr.mont. Dr.rer.nat Michael Fischlschweiger

Graz, January 2018

AFFIDAVIT

I declare that I have authored this thesis independently, that I have not used other than the declared sources/resources, and that I have explicitly indicated all material which has been quoted either literally or by content from the sources used. The text document uploaded to TUGRAZonline is identical to the present master's thesis.

Date

Signature

Abstract

The requirement to inspect materials and components for defects and inhomogeneities is a must in the industry as well as research to verify new materials or to ensure the safety of these components. Non-destructive (NDT) testing utilizes various physical effects to test materials and components without damaging the material or component. Active thermography uses heat transfer into the material and records it with an infrared camera. The advantage of this principle is a non-contact, spatially resolved and rapid thermal measurement process that represents inhomogeneities in a material due to interaction with a heat flux. The heat flow is generated by an externally controlled excitation source. In active thermography there are basically two forms of excitation, a pulsed excitation (Pulse Thermography PT) or a sinusoidal excitation (Lock-In Thermography). In this work, mainly the pulse thermography is presented and used.

If a material or component is excited with an external excitation source and has inhomogeneous illumination, it may be difficult to visualize these flaws and inhomogeneities. In order to increase the contrast between inhomogeneities and homogeneous background, algorithms are presented which increase this contrast. Algorithms are developed which require a choice of error-free background and an algorithm derived from the one-dimensional heat equation.

If defects and inhomogeneities in the material are discovered, the question of the depth in the material, at which the defect is present, arises. To calculate this, three different algorithms are studied (LSD, APST and Maximum Contrast). In order to implement these, methods have to be developed to remove the noise of thermography sequences. One of these methods used in active thermography is Thermographic Signal Reconstruction (TSR), which is based on the principle of polynomial fit.

Furthermore, different numerical methods of the heat equation are implemented with the help of finite differences. By simulating the cooling process, the inhomogeneous background can be compensated by subtracting the simulation from the thermographic sequence. The simulation of the heat equation is also a requirement to implement the algorithm Maximum Contrast for depth determination.

In order to be able to implement the heat equation at all, the material-constant thermal diffusivity has to be determined. In order to determine this, the method of laser flash analysis is applied and implemented for active thermography.

Keywords: *NDT, Active Thermography, Thermal diffusivity, Depth determination, Heat equation, Model-based analysing, Feature extraction*

Zusammenfassung

Um die Sicherheit von Komponenten und Werkstoffen zu gewährleisten, wird in der Industrie sowie Forschung immer mehr Wert auf die Prüfung dieser Komponenten und Werkstoffen gelegt. Ziel solcher Prüfungen ist es, Defekte, Inhomogenitäten sowie physikalische Werkstoffparameter zu extrahieren um Aussagen über die Verwendbarkeit sowie Einsatzgrenzen zu erhalten. Die zerstörungsfreie Prüfung befasst sich mit der Extrahierung solcher Parameter und nutzt dazu verschiedene physikalische Effekte um diese Extrahierung zu ermöglichen. Aktive Thermografie nutzt dabei den physikalischen Effekt der Wärme, welche in das Material mit einer externen Erregerquelle eingebracht wird. Dieser Wärmefluss kann in der Aktiven Thermografie hauptsächlich in zwei verschiedene Wege eingebracht werden, einerseits durch einen einzelnen Wärmeimpuls (Pulse Thermography PT) und andererseits durch eine periodische Erregung (Lock-In Thermography). Der anschließende Abkühl- oder Erwärmungsvorgang wird dabei mit einer Thermografiekamera aufgenommen. Durch die Interaktionen des Wärmeflusses mit Fehlstellen resultieren dadurch verschiedene, und durch verschiedene Inhomogenitäten, charakteristische Abkühl- oder Erwärmungskurven. In dieser Arbeit wird der Fokus überwiegend auf die Erregerform der PT eingegangen.

Werden Komponenten und Werkstoffe mit einer Erregerquelle erregt, welche keine homogene Ausleuchtung erzielt, kann es bei der Betrachtung des Thermograms zu Schwierigkeiten kommen, um Inhomogenitäten vom fehlerfreien Hintergrund zu unterscheiden. Algorithmen wurden dabei implementiert, um diesen Effekt der inhomogenen Ausleuchtung zu kompensieren.

Weiters werden Methoden vorgestellt, die bei Verwendung der aktiven Thermografie häufig Anwendung finden um Inhomogenitäten und Defekte zu extrahieren.

Wurden Defekte und Inhomogenitäten in Komponenten gefunden, ist ein weiteres Ziel die Tiefe dieser Inhomogenitäten zu bestimmen. Dazu wurden drei verschiedene Algorithmen erforscht (LSD, APST und Maximum Contrast). Um diese Algorithmen implementieren zu können besteht die Anforderung von zeitlich rauschfreien Thermogrammen. Um dies zu ermöglichen wurde die Methode Thermographic Signal Reconstruction (TSR) implementiert, welche auf dem Prinzip der Polynom Approximation basiert.

Durch Simulation des Abkühlvorganges mittels Finiter Differenzen der Wärmeleitgleichung wird die inhomogene Erregung kompensiert. Dabei wird die inhomogene Erregung mit der Simulation des Abkühlvorganges subtrahiert und der Kontrast zwischen Inhomogenitäten und fehlerfreiem Hintergrund erhöht. Weiters ist die Simulation des Abkühlvorganges Ausgangspunkt der Maximum Contrast Methode, welche für die Tiefenberechnung verwendet wird. Um die Wärmeleitgleichung sowie Tiefen von Inhomogenitäten berechnen zu können muss der physikalische Parameter, Thermische Diffusivität α , bekannt sein. Um diesen Parameter zu ermitteln, wird die Methode der Laser Flash Analyse angewendet und für die Aktive Thermografie adaptiert.

Keywords: *NDT, Active Thermography, Thermal diffusivity, Depth determination, Heat equation, Model-based analysing, Feature extraction*

Contents

1	Introduction	9
1.1	Motivation	9
1.2	Nondestructive Testing NDT	10
1.2.1	Classical methods of NDT	10
1.3	Problem Statement	17
1.4	Objectives and Approaches	17
2	Literature Review	19
2.1	Infrared Thermography	19
2.1.1	Electromagnetic Spectrum Bands	19
2.1.2	Black Body Radiation	21
2.1.3	IR Detectors and Sensor	23
2.1.4	IR cameras	24
2.1.5	Passive and Active Thermography	25
2.1.6	Excitation Sources	27
2.2	Mathematical Background	28
2.2.1	Partial Difference Equation	28
2.2.2	Derivation of heat equation in 1 dimension	30
2.2.3	Numeric of partial differential equations	32
2.3	Overview of most used Algorithms for Feature Extraction	34
2.3.1	Pulsed Phase Thermography (PPT)	34
2.3.2	Wavelet Transformation	35
2.3.3	Principle Component Thermography (PCT)	38
2.3.4	Statistical parameters	39
2.4	Related work on depth estimation	41
2.4.1	Log Second Derivative (LSD)	41
2.4.2	Absolute Peak Slope Time (APST)	42
3	Preprocessing Techniques	44
3.1	Fixed Pattern Noise (FPN)	44
3.2	Bad Pixel	44
3.3	Signal fitting	44
4	Processing Techniques	46
4.1	Thermographic Signal Reconstruction (TSR)	46
4.2	Contrast Methods	47
4.2.1	Absolute Contrast	48
4.2.2	Running Contrast	48
4.2.3	Normalized Contrast A	49

4.2.4	Normalized Contrast B	49
4.2.5	Standard Contrast	49
4.2.6	Differentiated Absolute Contrast (DAC)	49
4.3	Determination of the thermal diffusivity α	50
4.4	Implementation of heat equation	51
4.4.1	Explicit procedure	51
4.4.2	Implicit procedure	53
4.4.3	Cranck-Nicolson procedure	54
4.4.4	2-dimensional heat equation	54
4.4.5	Determination of the initial condition	56
4.4.6	Boundary conditions	57
4.5	Depth determination with new approach	58
4.5.1	Maximum Contrast	58
5	Experiment Setup	59
5.1	Used IR-camera	59
5.2	Used Flash lamp/Power supply	59
5.3	Software	60
5.4	Test specimen	60
5.4.1	Test specimen for testing the stability of the thermal diffusivity α	60
5.4.2	Test specimen for depth estimation	60
6	Experiments and Results	64
6.1	Experiments and results of the implemented Contrast Methods	64
6.2	Determination of the thermal diffusivity α	68
6.3	Implementation of Heat equation with finite differences	77
6.3.1	1D-Heat equation with explicit method	77
6.3.2	1D-Heat equation with implicit method	77
6.3.3	2D-Heat equation with explicit method	78
6.3.4	2D-Heat equation with implicit method	79
6.4	Depth determination	81
6.4.1	Preliminary observation	81
6.4.2	LSD - depth determination	84
6.4.3	APST - depth determination	89
6.4.4	Maximum Contrast	93
7	Conclusion and Discussion	95
7.1	Discussion of the results	95
7.1.1	Contrast methods	95
7.1.2	Determination of the thermal diffusivity α	96

7.1.3	Implementation of the heat equation	97
7.1.4	Depth determination	98
7.2	Conclusion	99

List of Figures

1	Example of Ultrasonic Resonanz testing [10].	11
2	Response of an ultrasonic pulse [13].	12
3	Example of Visual testing VT [14].	13
4	Example of Penetrate testing PT [8].	13
5	Example of X-ray inspection [9].	14
6	Functionality of MT [7].	15
7	Example Figure after IRT [6].	15
8	Flow chart of the thesis	18
9	Electromagnetic spectrum of light [11]	20
10	Transmittance of atmosphere in the range of 0 <i>um</i> to 15 <i>um</i>	21
11	Black body radiation as a function of wavelength for various absolute temperature [15]	22
12	Absorption by Non-transparent bodies	23
13	Transmittance by transparent bodies	23
14	Acquisition of the movement of a car wheel with a cooled camera [1]	25
15	Acquisition of the movement of a car wheel with an uncooled camera [1]	25
16	Overview of Thermography types	25
17	Cooling process of a non-defect (blue) and defect (red) area	27
18	Schematic image of the assumptions to derive the heat equation	30
19	Section of bar	31
20	Schematic representation of PPT [23].	35
21	Frequency resolution STFT	36
22	Frequency resolution of Wavelet transform	36
23	Schematic representation of DWT - Level 3 [3].	37
24	Schematic representation of SVD	38
25	Cumulative distribution function CDF of a random variable X [58]	39
26	Probability density function PDF of a random variable X [58]	40
27	Schematic principle of active thermography	41
28	Practical example of active thermography	41
29	Original thermographic signal in logarithmic scale	47
30	TSR-signal in logarithmic scale	47
31	Thermogram of a non-uniform excited specimen	48
32	Thermogram of a compensated non-uniform excitation	48
33	Positions of artificially introduced inhomogeneities	61
34	Dimension and arrangement of drills - PEHD	62
35	Gradiation of depths - PEHD	63

36	Original thermogram at 5 seconds after excitation	65
37	Original thermogram at 10 seconds after excitation	65
38	Thermogram manipulated with Absolute Contrast at 5 seconds after excitation	65
39	Thermogram manipulated with Absolute Contrast at 10 seconds after excitation	65
40	Thermogram manipulated with Running Contrast at 5 seconds after excitation	66
41	Thermogram manipulated with Running Contrast at 10 seconds after excitation	66
42	Thermogram manipulated with Normalized Contrast A at 5 seconds after excitation	66
43	Thermogram manipulated with Normalized Contrast A at 10 seconds after excitation	66
44	Thermogram manipulated with Normalized Contrast B at 5 seconds after excitation	67
45	Thermogram manipulated with Normalized Contrast B at 10 seconds after excitation	67
46	Thermogram manipulated with Standard Contrast at 5 seconds after excitation	67
47	Thermogram manipulated with Standard Contrast at 10 seconds after excitation	67
48	Thermogram manipulated with DAC at 5 seconds after excitation	68
49	Thermogram manipulated with DAC at 10 seconds after excitation	68
50	Inhomogeneous illumination and areas to test stability and correctness of α	69
51	Inhomogeneous illumination and areas of PA6-GF specimen α	72
52	Thermogram 5 seconds after excitation with subtracted heat simulation	77
53	Temporal profile of flawless background, drill in 1mm depth, drill in 0.5mm depth and GF-Tape	77
54	1D Explicit method - Initial condition	78
55	1D Explicit method - Stability condition	78
56	1D Implicit method - Initial condition	78
57	1D Implicit method - Stability condition	78
58	2D Explicit method - Initial condition	79
59	2D Explicit method - Stability condition with violated stability condition	79
60	2D Implicit method - Initial condition	80

61	2D Implicit method - Stability condition	80
62	Temporal profile of flawless background and inhomogeneity in 0.02mm depth	81
63	Temporal profile of flawless background and inhomogeneity in 0.24mm depth	81
64	Temporal profile of flawless background and inhomogeneity in 0.5mm depth	82
65	Temporal profile of flawless background and inhomogeneity in 0.72mm depth	82
66	Temporal profile of flawless background and inhomogeneity in 0.92mm depth	82
67	Temporal profile of flawless background and inhomogeneity in 1.11mm depth	82
68	Temporal profile of flawless background and inhomogeneity in 1.27mm depth	82
69	Temporal profile of flawless background and inhomogeneity in 1.5mm depth	82
70	Temporal profile of flawless background and inhomogeneity in 1.75mm depth	83
71	Temporal profile of flawless background and inhomogeneity in 2.02mm depth	83
72	Temporal profile of flawless background and inhomogeneity in 2.16mm depth	83
73	Temporal profile of flawless background and inhomogeneity in 2.25mm depth	83
74	Noise free simulated signal and TSR with an inhomogeneity of 2mm	84
75	Determined depth with LSD of inhomogeneity with numerical and analytical derivation	84
76	Simulated signal with a SNR of $20dB$ and TSR with an inho- mogeneity of 2mm	85
77	Determined depth with LSD of inhomogeneity with numerical and analytical derivation	85
78	Simulated signal with a SNR of $20dB$ and TSR with an inho- mogeneity of 3mm	85
79	Determined depth with LSD of inhomogeneity with numerical and analytical derivation	85
80	Schematic representation of depth estimation with LSD - PP- GF 2mm	86
81	Cooling curves of flawless background and drill in 2mm depth - PP-GF 4mm	87

82	Noise free simulated signal and polynomial fit with an inhomogeneity of 2mm	89
83	Determined depth with APST of inhomogeneity with numerical and analytical derivation	89
84	Simulated signal with a SNR of $20dB$ and polynomial fit with an inhomogeneity of 2mm	90
85	Determined depth with APST of inhomogeneity with numerical and analytical derivation	90
86	Simulated signal with a SNR of $20dB$ and a polynomial degree of 19 with an inhomogeneity of 3mm	90
87	Determined depth with APST of inhomogeneity with numerical and analytical derivation	90
88	Schematic representation of depth estimation with APST - PP-GF 2mm	91
89	Schematic representation of depth estimation with Maximum Contrast - PP-GF 2mm	93

List of Tables

1	Overview of advantages and disadvantages of NDT-Methods .	16
2	Overview of photoelectric sensors and thermal sensors [2] . . .	24
3	Overview of cumulants	40
4	Specification of <i>IR 8300 hp</i>	59
5	Specification of flash lamp	59
6	Specification power supply	60
7	Positions and kinds of inhomogeneities	61
8	Thermal diffusivity α of specimen PE-HD -2mm	69
9	Thermal diffusivity α of specimen PE-HD -3mm	70
10	Thermal diffusivity α of specimen PE-HD -5mm	70
11	Thermal diffusivity α of specimen PE-HD -8mm	71
12	Thermal diffusivity α of specimen PE-HD -10mm	71
13	Overall mean and standard deviation of PE-HD	71
14	Thermal diffusivity α of specimen PA6-GF 2mm -15cm flash distance	73
15	Thermal diffusivity α of specimen PA6-GF 2mm -25cm flash distance	73
16	Overall mean and standard deviation of PA6-GF - 2mm	74
17	Thermal diffusivity α of specimen PA6-GF 4mm -15cm flash distance	74
18	Thermal diffusivity α of specimen PA6-GF 4mm -25cm flash distance	75
19	Overall mean and standard deviation of PA6-GF - 4mm	75
20	Depth calculation with LSD - PP-GF 2mm	86
21	Depth calculation with LSD - PA6-GF 2mm	87
22	Depth calculation with LSD - PA6-GF 4mm	87
23	Depth determination of PE-HD plate with LSD	88
24	Depth calculation with APST - PP-GF 2mm	92
25	Depth calculation with APST - PA6-GF 2mm	92
26	Depth calculation with APST - PA6-GF 4mm	92
27	Depth determination of PE-HD plate with APST	92
28	Depth calculation with Maximum contrast - PP-GF 2mm . . .	94
29	Depth calculation with Maximum Contrast - PA6-GF 2mm . .	94
30	Depth calculation with Maximum Contrast - PA6-GF 4mm . .	94
31	Depth determination of PE-HD plate with Maximum Contrast	94

1 Introduction

1.1 Motivation

Non-destructive Testing NDT is the *art* to proof materials and components non-invasive based on physical principles. These principles depend on visual, oscillate mechanical, acoustic, electromagnetic and thermal base. On the basis of this physical principles, techniques were invented to extract inhomogeneities and defects to classify the quality of produced materials and components [18].

Accidents in everyday life, aviation, transportation and shipping reveal that the reliable characterization of materials and components and their modifications is an important prerequisite for safe operation. Therefore, damage must be detected in time so as to avoid failure. For reasons of time and cost, however, components are not to be exchanged unnecessarily in advance. Hence, a test method has to be found to inspect the used materials. NDT therefore offers important features to fulfil given requirements as e.g. inspection of different materials (composite material, metal), fast and extensive measuring procedure, reliable detection of delaminations, inclusions and other defects, non-contact measuring procedure and, if required, inspection result as image [74].

In the selection of the NDT methods, it is crucial that the interaction with the desired error is as strong as possible. In addition, it plays a major role whether the process provides "on-the-spot" in a harsh and possibly inaccessible environment, quickly and reliably, which are indisputable against disturbances or misinterpretation.

In this thesis *active infrared thermography* was chosen as NDT-technique to detect non visible inhomogeneities of materials and components. In contrast to conventional thermography (passive thermography), in active thermography heat flow is controlled by a controlled external energy source, e.g. flashlight, heat radiator, hot air, laser. On the base of interaction of the heat flow and the specimen, inhomogeneities and defects should be detected .

1.2 Nondestructive Testing NDT

The main goal of NDT is the inspection, testing or evaluation of components and constructions to materials for discontinuities or inhomogeneities without changing or destroying the serviceability of the inspected component or construction [29]. These discontinuities or inhomogeneities usually occur during the production of the object and can influence the lifecycle of the tested specimen. In general, the application of NDT fulfills three important points:

- Avoiding hazards for people and environment
- Ensuring function standby
- Early selection of defective components and constructions

The analogy of NDT can be found in medical diagnostic as e.g. the sonography of hips of sucklings. Therefore, this method is used to detect dislocated or too small hips without any risks of impairment due to the applied examination methods [45]. But also simpler methods can be used (e.g. visual inspection) to detect inhomogeneities of components and constructions without destroying the component. Nowadays, there are a lot of nondestructive test methods and it would go beyond the scope of this thesis to review them all. Nevertheless the "classical" methods are presented and briefly described in the following section.

1.2.1 Classical methods of NDT

Concerning the classical methods of NDT we can differentiate between acoustic methods [40] and methods where we exploit the properties of electromagnetic waves [33]. Acoustic Methods use the properties of mechanical waves, which are with increasing frequency: ring test or sound analysis and ultrasonic resonance inspection [34].

Acoustic test techniques

Acoustic test techniques are one of the oldest test methods to detect inhomogeneities or defects of components and constructions. These methods can be executed in an audible frequency spectrum (<16 kHz), then it is called *ring test* or *sound analysis* [5], as well as in a not audible frequency spectrum (>16 kHz), then it is called *ultrasonic resonance inspection* [5]. In general, acoustic test techniques are methods which are volume-oriented and evaluate

the quality of whole components and constructions [40].

In principle, acoustic test techniques use the physical effect, that after acoustic excitation a solid state body oscillates in its natural resonance. This natural resonance is like a fingerprint of the tested component or construction. The natural resonance can be detected with a sensor, analysed and compared with a reference value (see Figure 1). After comparison, the component or construction can be evaluated and when necessary discarded. To be able to make statements about the relation of the resonance frequency and a reference frequency one of the most important requirements is to hold the test conditions constant [48].

A possible test procedure can be

- Excitation of a oscillate-able mounted test specimen
- Frequency measurement
- Extracting of test specimen specific values
- Comparison of specific values with reference values
- Classification of test specimen

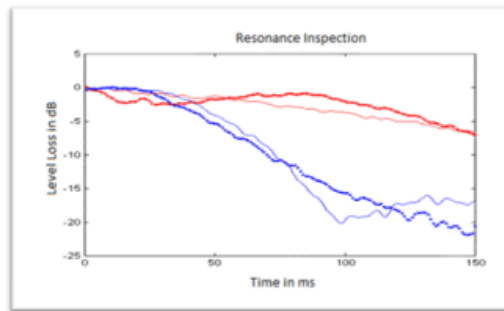


Figure 1: Example of Ultrasonic Resonanz testing [10].

The principle **Ultrasonic Test UT** can be used for almost all kinds of materials or components. Therefore, ultrasonic waves are induced into the specimen with a transducer. At inhomogeneities these ultrasonic waves are reflected and are recorded with a receiving transducer. In most of the ultrasonic test units first the transducer works as transmitter and after transmission the transducer works as receiver [95]. Measuring transit time it can be deduced to inhomogeneities as you can see for example in Figure 2. In modern ultrasonic test units it is also possible to measure the geometries of the detected inhomogeneities of the tested specimen [79]. One of the main

advantages of this method is that test depths of several meters are possible, depending on the acoustical property of the specimen. In order to reliably determine the position and size of the inhomogeneities, the transducer must be positioned perpendicular to the inhomogeneity. The resolution of this method depends on the used ultrasonic transducer and is limited by half of the ultrasound pulse [79]. To correctly interpret ultrasound images, trained personnel must be used.

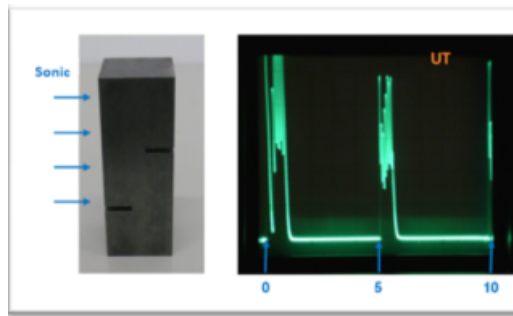


Figure 2: Response of an ultrasonic pulse [13].

Spectrum of Nondestructive test methods with electromagnetic waves

The most famous inspection method is **Visual Testing (VT)** (see Figure 3 for an example) which is used for e.g. production of electronic printed circuit board, food industry or as combination with other test methods to detect inhomogeneities. This inspection method was standardized in ISO 9712 and in DIN EN 13018 [68] [36] [75]. In DIN EN 13018, they differentiate between direct visual testing and indirect visual testing. Direct visual testing is without interruption of the light path between test surface and eye of the observer and can also be distinguished between direct visual testing without aid (= observation of test surface with the unaided eye) and direct visual testing with aid (= observation with aid e.g. endoscopy, magnifying glass or mirror). Typical inhomogeneities or defects which should be detected are on the surface of components or constructions and are e.g. mechanical defects (scratches, cracks), sediments, defective mounting, burr formation and also color changes [75].

One other Nondestructive test method is **Penetrate testing PT** [19] to visualize inhomogeneities and defects which are opened to the surface of the tested specimen (see Figure 4). This test method can also be distinguished



Figure 3: Example of Visual testing VT [14].

between liquid penetrant inspection [72] and fluorescent pentrant inspection [54]. By liquid penetrant inspection [72] the specimen is coated with red penetrant and after the end of the waiting time, the specimen is cleaned and coated with a fine grained powder. This powder extract the rest of the penetrant in the cavities. The big contrast of the powder and the penetrant provides the detection of defects and cracks. On the other hand, by fluorescent pentrant inspection the specimen is injected with fluorescent pentrant. After the end of the waiting time, the specimen is classified under UV-light [54].



Figure 4: Example of Penetrate testing PT [8].

The next method **X-ray inspection RT** is used for two and three dimensional testing of components and constructions to visualize inhomogeneities that can also be inside the tested specimen. Constructions and components

are radiographed with high energy electromagnetic rays as X-rays and gamma rays. These electromagnetic rays are alleviated difference with variation of thickness of the tested specimen and visualize the radiographed energy in gray scale [89]. Hence, with this method inhomogeneities like delaminations, cracks and a lot of more inhomogeneities can be found also inside the tested specimen. Disadvantages of this test method are that only limited thickness can be tested, it is very time expensive, radiation hazard for humans and employees, who need special training, as well as for the specimen itself [61]. An example of RT can be seen in Figure 5.

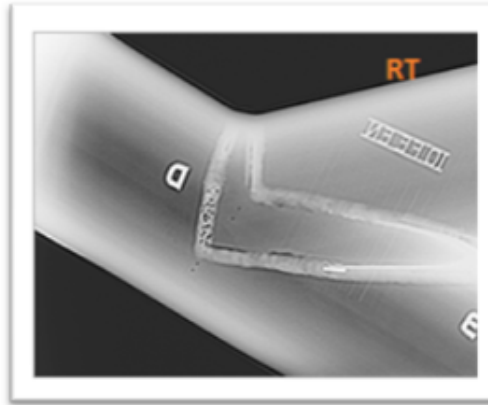


Figure 5: Example of X-ray inspection [9].

Magnetic leakage flux test MT is used to find cracks on the surface as well as to find local cross section reduction or thickness changes in ferromagnetic materials. Therefore the specimen is magnetized and the resulting magnetic flux lines deviate parallel to the surface. Are inhomogeneities like cracks on or near to the surface, these inhomogeneities produce a stray magnetic field and the magnetic flux lines leave the ferromagnetic material on the one side of the defect and enter on the other side of the material and produce magnetic poles. If magnetic powder is distributed across the surface of the specimen, the powder is accumulated on the inhomogeneities because of the magnetic effect. This principle only works for inhomogeneities that are transverse to the magnetic flux lines. Furthermore inhomogeneities like cracks can only be detected that are in a certain depth[19]. Figure 6 shows an example of the functionality of MT.

The last, but in this thesis the most important Nondestructive test method that is mentioned is **Active Thermography** or **Infrared Thermography**

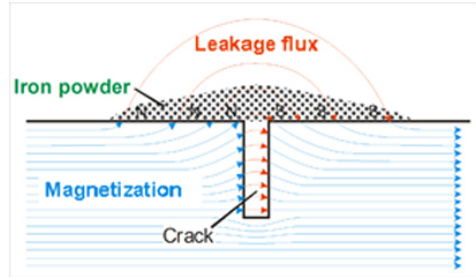


Figure 6: Functionality of MT [7].

IRT. In the case of active thermography, a heat flow is induced by the energetic excitation of components or constructions. Inhomogeneities or defects inside the test specimen influence the resulting heat flow. High precision cameras capture the heat flow on the surface of the specimen. The influenced heat flow through inhomogeneities causes a difference on temperature on the surface as in areas without inhomogeneities [81]. With different algorithms like *Pulse Phase Thermography*, *Statistical Parameter*, *Wavelet Transform* or *Principal Component Analyse* inhomogeneities and defects can be visualized in final images [47] as can be seen for example in Figure 7.

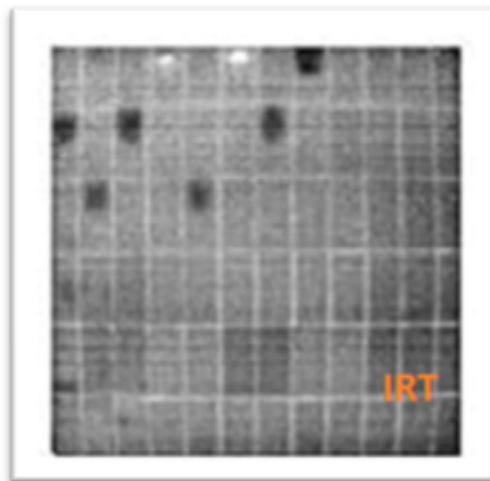


Figure 7: Example Figure after IRT [6].

It can be seen that a lot of NDT-methods exists, a short overview of the advantages and disadvantages of the above described NDT-methods can be seen in table 1.

Table 1: Overview of advantages and disadvantages of NDT-Methods

	Advantage	Disadvantage
Resonance Inspection	Fast Whole part test No preparation of the specimen required	Only materials that resonate Location of defect can not be found Large specimen difficult to test
Ultrasonic Testing	Very sensitive to cracks Measurement of thickness of specimen Measurement of geometry of defect	Couplant required Trained operators Complex specimen may be difficult to test
Visual Testing	Very Fast Low cost No preparation of the specimen required	Only surface can be checked
Penetrate Testing	Low cost Portable	Only defects that are open to the surface can be detected Messy Costly Cleaning of the specimen
X-ray Inspection	Detection of surface and internal defects No specimen preparation Good resolution	Hazardous to humans Trained operators Slow Expensive
Magnetic leakage flux	Low cost Surface and internal defects can be detected Portable	Ferromagnetic materials only Demagnetization after testing Knowledge about tight alignment of magnetic field
Active Thermography	Large area can be tested Allows recording in real time Risk-free Detection of surface and internal defects	Quality depends on heat diffusion of the specimen Limited thickness of the specimen can be tested Measurement of geometry of inhomogeneities

1.3 Problem Statement

Active Infrared Thermography is a non-destructive testing method that uses an excitation source to induce a heat flow into the specimen [78]. Are inhomogeneities inside the specimen, they cause a disturbance of the heat flow and leads to a difference in the cooling or heating process at the surface in relation to the defect free environment. The prerequisite for detecting inhomogeneities is that the excitation source is energetically capable of bringing the test object out of the basic temperature state. If this temporal interaction between heat and test object is recorded with an infrared camera, inhomogeneities such as cracks, cavities or delaminations can be visualized using suitable evaluation algorithms [63]. Many of these Algorithms are sensitive to inhomogeneous heating due to non-uniform illumination. If algorithms are used which are sensitive to inhomogeneous illumination, this must be compensated.

If inhomogeneities have been successfully identified, further requirements arise for the system such as determination of the depth of inhomogeneities. The principle of active thermography is a physical process and the result is strongly influenced by the material properties. The most important material parameter to extract the depth is the thermal diffusivity α . If this parameter is not known, a method must be found to determine it.

1.4 Objectives and Approaches

Figure 8 describes the goal of this work by means of a flowchart.

Standard algorithms are used for preprocessing to suppress camera image sensor-specific image errors, such as fixed pattern noise or bad pixels, in order to suppress corruption of the thermogram [99]. If excitation sources are used which do not achieve homogeneous illumination, they can have a massive influence on the quality of the algorithms for feature extraction. Algorithms are introduced and implemented to compensate this inhomogeneous illumination. Furthermore, the quality of the individual methods is shown. In order to extract inhomogeneities of a thermographic sequence, the most commonly used algorithms for feature extraction are described.

If the requirement of inhomogeneities exists to determine the depth, the parameter of thermal diffusivity is needed. If the parameter α is not given, a method for determining this parameter α is described. Furthermore, two well-known algorithms (LSD, APST) for depth calculation are implemented and their quality checked. These two known algorithms are compared with a newly developed method, called *Maximum Contrast*.

Finally one is able to go through the presented flowchart with all necessary

input parameters.

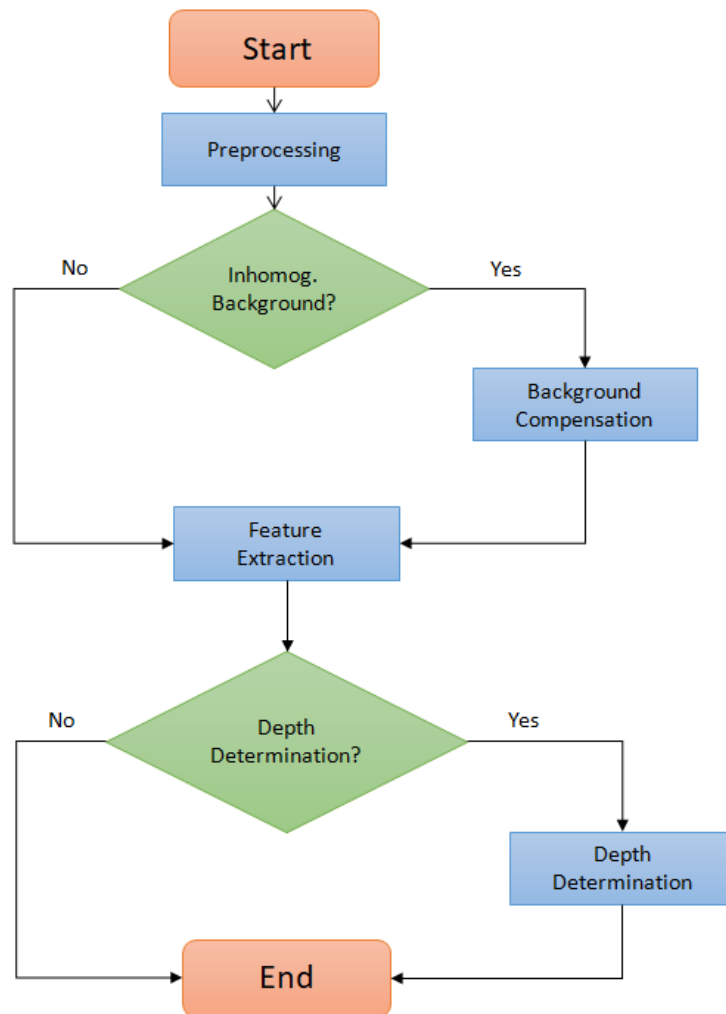


Figure 8: Flow chart of the thesis

2 Literature Review

2.1 Infrared Thermography

The first thermographic systems were developed and used by the military in the second world war [26]. Since then, these systems have been further developed and found new fields of application, such as in medicine for the investigation of the body temperature of humans, in agriculture for the investigation of frost sensitive plants, in maintenance for monitoring of temperature and thermal patterns on pumps or motors [69]. The potential of this new technology for NDT was quickly recognized and was first used in the 1960s as NDT technology and played a major role in quality control and service control. As can be seen, infrared thermography has a long history and has been further developed over the last 60 years and still plays a major role in industrial applications as well as in commercial applications [59].

Infrared thermography consists of a series of components with the core element of the infrared camera which makes the invisible infrared rays visible for human. [50]. The intensity of the invisible infrared ray emanating from a point is interpreted as a measure of its temperature. The infrared camera has the task of displaying the intensities as a map or image as false colors or grayscale. By analyzing the contrast of the map or image, statements about the quality of the examined object can be made or inhomogeneities detected [50].

There are different devices or components that detect invisible infrared light. An infrared sensor [51] consists of a temperature-sensitive pyrosensor which reacts to temperature changes and generates an electrical voltage. the generated voltage is proportional to the temperature. The difference to an infrared camera is that the camera consists of an array of sensors [76] and has the ability to detect infrared rays from different spatial points at the same time. The output of the sensor array can be represented as false color map or grayscale image.

2.1.1 Electromagnetic Spectrum Bands

Light is a form of electromagnetic radiation and can be generally separated for humans in visible light and invisible light. An overview of the spectrum of light can be seen in figure 9 where for humans the visible region is between 380nm and 780nm [46].

The infrared radiation was discovered by Friedrich William Herschel in 1800 [16]. He used a glass prism to spectrally decompose the light. As you can see in figure 9, infrared radiation is above the visible wavelength range.

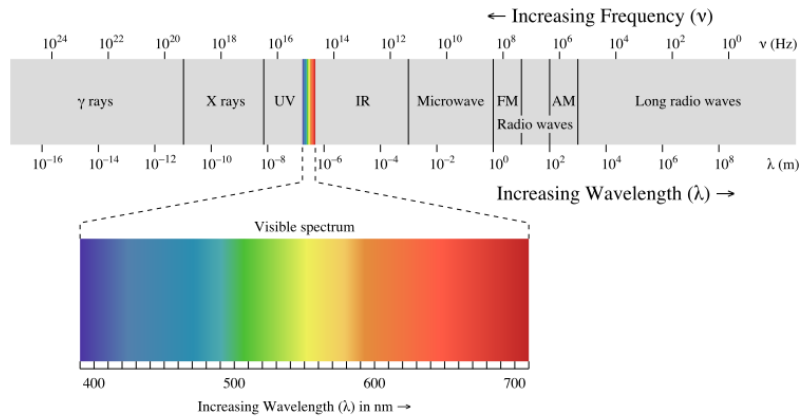


Figure 9: Electromagnetic spectrum of light [11]

Infrared radiation is electromagnetic radiation, which is connected to the visible radiation in the direction of larger wavelengths and extends to the microwaves [71]. It covers a wavelength range from 780 nanometers to 1 millimeter. The infrared radiation is in turn divided into several subregions [71].

The near-infrared (NIR) region extends over the electromagnetic spectrum from 780 nm to $1.4\mu\text{m}$ and attaches itself to the visible light. In remote sensing, this area is used to analyze vegetation using aerial and satellite imagery.

The next range of infrared radiation is the short-wave infrared radiation (SWIR) which is divided in the range of 1.4μ to 3.0μ .

The next region, mid-wavelength infrared range (MWIR), extends over the range of thermal radiation at terrestrial temperatures and is in the wavelength range between $3\mu\text{m}$ and $8\mu\text{m}$.

Long-wavelength infrared (LWIR) is the region which is in the range of 8μ to 15μ and is helpful in observing and clearing up in the dark or in poor visibility without the need for residual light and is mostly used in non-destructive testing, medical applications and safety technology.

The last range of infrared radiation is the far infrared (FIR) range which has the longest wavelength range of infrared radiation. FIR covers the wavelength range of $15\mu\text{m}$ to $1000\mu\text{m}$.

At the gas mixture of the atmosphere, the air, which contains various gases such as ozone, carbon dioxide and water vapor, the electromagnetic infrared radiation is absorbed or scattered depending on its wavelength. Those results in an atmospheric window, which show how permeable the electromagnetic radiation is, depending on its wavelength (see figure 10) [91][38].

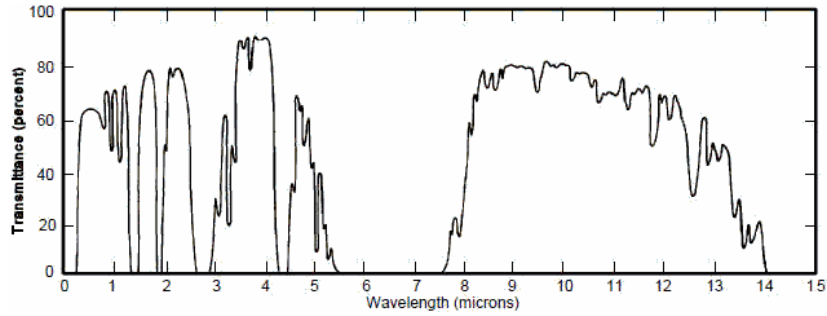


Figure 10: Transmittance of atmosphere in the range of 0 μm to 15 μm

2.1.2 Black Body Radiation

The German physicist Gustav Robert Kirchhoff described the correlation between absorption and emission of a real body in thermal equilibrium in 1859, which states that bodies which absorb the temperature radiation well, and also emit temperature radiation well [64]. A black body or black radiator is thus an idealized source of thermal radiation. Such bodies completely absorb and radiate temperature radiation completely. Hence no body emits or absorbs more energy than a black body. In other words, when a black body absorbs a temperature radiation of amount, it also emits a temperature radiation of the same amount. Furthermore a black body is a diffuse emitter and thus a function of temperature and wavelength and independent of the direction of irradiation [87].

Each body over the absolute zero point $0\text{K} \hat{=} -273.15\text{C}$ emits electromagnetic radiation with different wavelength. The distribution of the radiation intensity to the individual wavelengths is described by *Planck's radiation law*. In 1900, Max Planck [64] succeeded in describing the distribution of the electromagnetic energy of the heat radiation of a black body as a function of the wavelength of the radiation as you can see in equation (1).

$$M_{\lambda}(T) = \frac{2\pi hc^2}{\lambda^5} (e^{\frac{hc}{\lambda kT}} - 1)^{-1} \quad (1)$$

where:

h = Planck constant

λ = Wavelength

T = Temperature

k = Boltzmann constant

c = velocity

In figure 11 you can see the spectral energy densities where each curve is seen to peak at a somewhat different wavelength. The radiation intensity of

the heat radiation, which is composed of electromagnetic waves with different wavelengths, is described by the Planck's radiation law. The resulting radiation intensity has a clear maximum. Wien's law [87] describes the shift of that peak in terms of temperature.

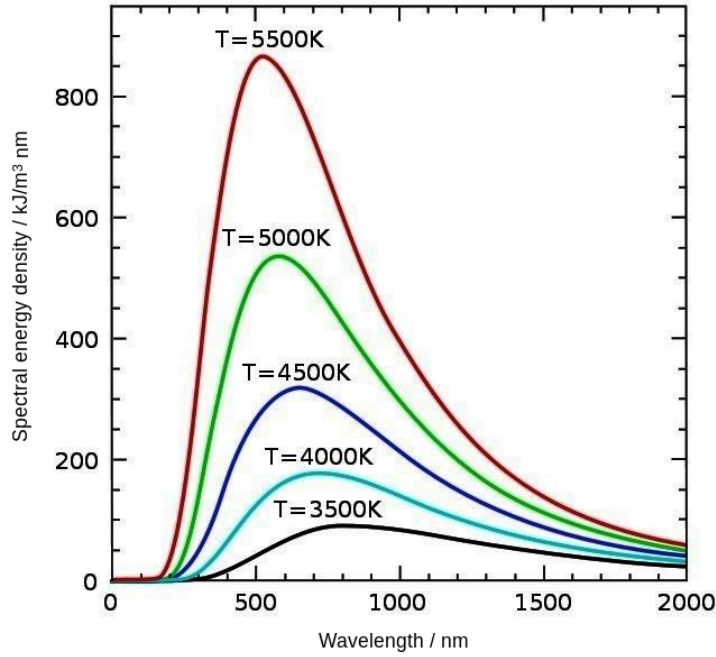


Figure 11: Black body radiation as a function of wavelength for various absolute temperature [15]

In the case of a real body, the radiation intensity on the surface can be reflected, absorbed or transmitted [41] in transparent bodies. The degree of reflection indicates the ratio of reflected radiation to the total radiation (2).

$$\frac{q_r}{q} = \frac{\text{reflected radiation}}{\text{total radiation}} \quad (2)$$

If only a part of the radiation is reflected, the remaining radiation passes through the body and is absorbed by non-transparent bodies (3) or transmitted by transparent bodies (4). Between these three variables (reflection, absorption, transmission) exists the relationship which sum equals 1.

$$\frac{q_a}{q} = \frac{\text{absorbed radiation}}{\text{total radiation}} \quad (3)$$

$$\frac{q_t}{q} = \frac{\text{transmitted radiation}}{\text{total radiation}} \quad (4)$$

Non-transparent Body

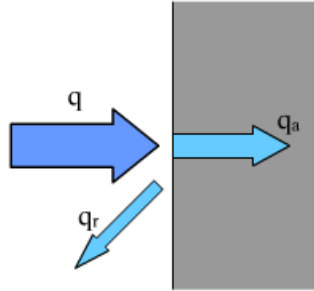


Figure 12: Absorption by Non-transparent bodies

Transparent Body

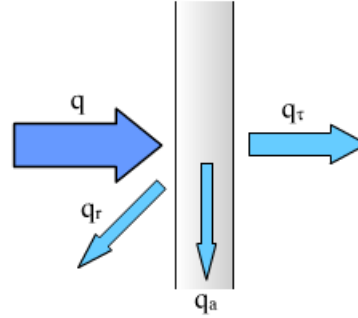


Figure 13: Transmittance by transparent bodies

2.1.3 IR Detectors and Sensor

At the heart of non-destructive testing by means of thermography is the optical component which receives infrared radiation without contact and converts it into a high-quality, measureable signal. To measure infrared radiation in a proper way there are basically two main types of IR detectors which are on the first hand thermal detectors [12] and on the other hand photonic detectors [92].

In case of a thermal detector [12], the energy is absorbed by the electromagnetic radiation to be detected in the receiver material. The resulting temperature increase in the detector is converted directly or indirectly into an electrical signal by the absorbed energy. For example, in a radiation thermocouple, the energy is converted directly into thermoelectric voltage. In the case of a bolometer, however, the energy arriving at the detector leads to the heating of metal. This causes the change in resistance and can thus be put into proportion. In both cases the electrical answer of the detector is proportional to the incoming energy. Such detectors are cheaper compared to photoelectric detectors, however, they have a lower sensitivity and larger time constant.

Photoelectric sensors [92] use the principle of inner photoelectric effect in semiconductors. Due to the energy of the incoming photons at the detector,

electrons are lifted from the valence band into the higher-energy conduction band and removed from the metal surface. The kinetic energy of the liberated photoelectrons depends linearly on the wavelength of the induced radiation [57]. Such detectors usually have a high sensitivity and a small time constant. The big disadvantage, however, is that these detectors often have to be cooled in order to reduce the intrinsic noise [56].

An overview of the advantages and disadvantages of thermal detectors and photoelectric sensors can be seen in table 2.

Table 2: Overview of photoelectric sensors and thermal sensors [2]

Photoelectric sensors	Thermal sensors
high sensitivity	wavelength independent sensitivity
very high temperature resolution (<25mk)	good temperature Resolution (>30 mk)
time constant: microseconds	time constant: milliseconds
extensive cooling technique	no cooling required
limited lifetime	long lifetime stability
expensive	low-cost

2.1.4 IR cameras

Thermography cameras are meant to detect the heat radiation of objects or bodies without contact and to display areal temperatures [73]. Focal plane arrays (FPAs) [76] are used to display areal temperature curves. The biggest difference between modern thermal imagers is whether detectors are cooled or not [2]. Choosing a thermography camera depends on the application requirement. Cooled detectors have some advantages compared to uncooled but cost is higher and the size of the camera is usually larger. If there is a requirement that smallest temperature differences have to be detected, high-speed recording is required, a very high sensitivity is required or only a part of a spectrum has to be detected, then it is better to purchase a cooled infrared camera [2]. However, uncooled thermal imaging cameras are much cheaper than cooled cameras and also significantly smaller in size, which results in better handling. An example of a cooled and uncooled camera can be seen in figure 14 and figure 15.



Figure 14: Acquisition of the movement of a car wheel with a cooled camera [1]



Figure 15: Acquisition of the movement of a car wheel with an uncooled camera [1]

2.1.5 Passive and Active Thermography

There are different types of thermography to achieve desired results. Basically, infrared thermography (IRT) can be divided into two types which are active and passive thermography. The application of active thermography can in turn be further subdivided. A rough overview can be found in figure 16 and will be described below.

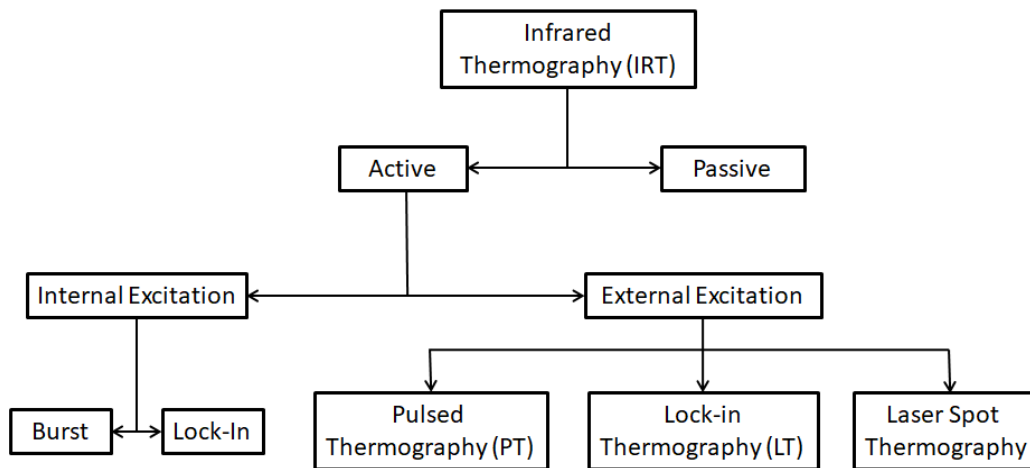


Figure 16: Overview of Thermography types

Passive Infrared Thermography: Each body above the absolute zero point of $0K \hat{=} -273.15C$ emits electromagnetic radiation with different wavelength [71]. Hence, every body above the absolute null point emits thermal radiation in form of electromagnetic radiation. This phenomenon is exploited in passive thermography in order to detect the temperature distribution of the object under test, which is caused by the environment or the process, without forced thermal excitation of the object [21]. This method is used, for example, in construction technology [83] to detect heat losses in buildings, in human medicine to detect inflammation or even breast cancer without burdening the patient with X-rays [32].

Active Infrared Thermography: Active Infrared Thermography is a non-destructive testing method that is more widely used than passive thermography to test specimen for inhomogeneities [63]. The difference to passive thermography lies in the fact that an external or internal excitation source applies a heat pulse to the object to be examined [21]. This heat pulse leads to a heat flow in the specimen. If there are inhomogeneities in the object, they cause a disturbance of the heat flow. This disturbance leads to a difference in the cooling or heating process at the surface in relation to the defect-free environment. If this temporal interaction between heat and test object is recorded with an infrared camera, inhomogeneities such as cracks, cavities or delaminations can be visualized using suitable evaluation algorithms [78]. To get a better understanding, figure 27 shows a cooling process of a defect free and a defect area. As you can see in figure 16, there are mainly three classical active thermographic techniques we can use if we use an external excitation source.

In pulse thermography, a heat flux is induced by a short pulse into the test object. This short heat pulse reaches the specimen surface and travels through the specimen. Inhomogeneities of the specimen lead to different temperatures with respect to non-defective areas. This evolution of cooling processes can be monitored with an IR-camera [63]. If a short excitation pulse is used the method is called *Pulse Thermography PT*. The *Lock-In Thermography* uses heat sources that can be modulated differently. Components to be examined are periodically excited with the help of these heat sources. If components are excited, for example sinus modulated the excitation frequency determines the depth from which information can be obtained [67]. An advantage of this method is that by averaging several heating periods, an improvement of SNR can be achieved [25].

When it comes to *Laser Spot Thermography* a high power laser source is used to deliver heat to a point at the surface. Inhomogeneities can be detected close to the delivered heat point [53].

Furthermore, there are two configurations for data acquisition. The first con-

figuration is the reflection mode where both, the heating and the recording, are performed from the same side. The second configuration is the transmission mode where the heating source is located on the back side and the recording source is located at the opposite side.

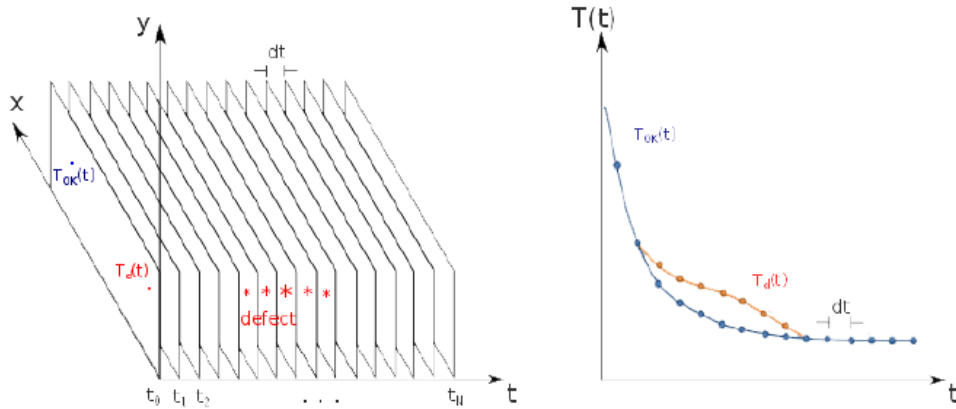


Figure 17: Cooling process of a non-defect (blue) and defect (red) area

2.1.6 Excitation Sources

In active thermography, one of the most important components is the excitation source. In figure 16, it is shown that either an internal excitation source or an external excitation source has to be used in order to be able to induce a heat flow into the object to be examined [28][78].

If active thermography with an internal excitation source [28] is used, a mechanical oscillator (sonic or ultrasonic transducer) is often applicable which is in direct contact with the object. If inhomogeneities are present, the energy, generated by the oscillator is dissipated in form of heat waves and can thus be recorded at the material surface.

An inductive excitation source [77] can be used in electro-conductive materials. Determined by the excitation frequency, eddy currents can be generated at a certain depth, depending on the excitation frequency. Defects in the specimen create a change in the eddy currents, which changes the temperature distribution. This change in the temperature distribution can in turn be recorded with an IR-camera and visualized [77].

If an external excitation source is used, optical sources are usually applicable. In pulse thermography, there is a requirement of a short pulse with high

energy which can be achieved with flash lamps [64]. When using Lock-In Thermography where modulated heat sources are usually required, halogen lamps are used at low frequency and intensity-modulated laser sources are used at higher frequencies [67].

2.2 Mathematical Background

2.2.1 Partial Difference Equation

If there is a desire to model processes in physics and engineering, very often differential equations are used [42]. If the sought solution depends only on one variable (space or time), one speaks of an ordinary differential equation [27]. Looking at equation (5) it quickly becomes apparent that one is looking for a function as a solution.

$$y' = 2y + x^2 \quad (5)$$

Many technical and physical processes cannot be described, or only in special cases, by one coordinate and ordinary differential equation. Thus, partial differential equations are needed. So if one has the case that the process spreads throughout the space and also propagates over time for transient problems, the solution is a function of several variables and the mathematical model is one or a system of partial differential equations [27]. For example, in unsteady flows the velocity and pressure are sought as functions as you can see in equation (6).

$$v = v(x, y, z, t), p = p(x, y, z, t) \quad (6)$$

The degree to which partial differential equations are divided is given by the highest derivative. The most general form of a partial differential equation of the second order is shown in formula (7).

$$F(x, y, u, u_x, u_y, u_{xx}, u_{xy}, u_{yy}) = 0 \quad (7)$$

Extending the construction of numerical methods from two-dimensional problems to three-dimensional problems is often just a simple transfer of the algorithms. However, the transition from the one-dimensional ordinary differential equation to the two-dimensional partial differential equation requires new ideas and approaches, which is usually more difficult [27]. Solutions of differential equations can show very different behaviour, depending on the problem. In case of partial differential equations, the behaviour differs and can roughly be divided into three classes, which fundamentally describe different physical processes [42].

- stationary procedures
- dissipative phenomena
- wave propagation processes

Classification of partial differential equation 2nd Order

To classify partial differential equations of second order, we start with equation (8) which is limited to two space dimensions. Furthermore, it is a prerequisite that the sought solution u depends on the independent variables x and y and that the solution is continuously differentiable at least twice.

$$a \cdot u_{xx} + b \cdot u_{xy} + c \cdot u_{yy} = h \quad (8)$$

If condition (9) is fulfilled, the equation (8) is called **linear with constant coefficients** or **quasilinear**

$$a \in \mathbb{R}, b \in \mathbb{R}, c \in \mathbb{R} \quad (9)$$

The linear differential equation of second order with constant coefficients can thus be divided into three categories: It's called **elliptical** if

$$b^2 - 4ac < 0 \quad (10)$$

it's called **parabolic**, if

$$b^2 - 4ac = 0 \quad (11)$$

and **hyperbolic**, if

$$b^2 - 4ac > 0 \quad (12)$$

are fulfilled.

Stationary states of equilibrium in various physical fields, such as strength theory, magnetostatics [35], fluid mechanics [94] or thermodynamics [80], is the area of application of **elliptic differential equations**.

One of the most important equations in this thesis, the heat equation, is described by a **parabolic differential equation**.

If the requirement is to describe unsteady processes, such as waves and propagation phenomena, **hyperbolic differential equations** are used [43].

2.2.2 Derivation of heat equation in 1 dimension

As described above, the heat equation is part of parabolic differential equation. This section describes the derivation of the relationship between the temporal and spatial changes in temperature at a location in a body. To derive the heat equation in 1 dimension, a thin bar of length L is given. Furthermore, we assume that the bar is of homogeneous material, straight, have uniform cross section and the sides of the bar are perfectly insulated. Hence, the temperature u is a function of position x and time t . Figure 18 schematically shows the assumptions [90].

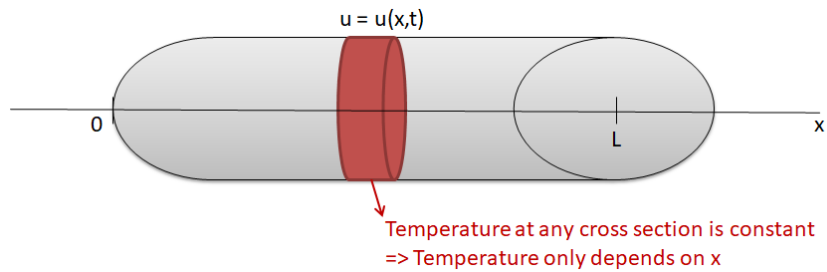


Figure 18: Schematic image of the assumptions to derive the heat equation

Now we want to show how to form the heat equation:

$$u_t = \alpha u_{xx} \quad (13)$$

where the thermal diffusivity α is given by:

$$\alpha = \frac{\kappa}{\rho c} \quad (14)$$

κ = Thermal conductivity

ρ = Density

c = Specific heat capacity

κ, ρ, c are positive constants and depend on the material of the bar.

Considering a section D of the bar with ends x_0 and x_1 , as can be seen in figure 19.

Now the total amount of heat $H = H(t)$ in D is:

$$H(t) = \int_{x_0}^{x_1} c\rho u(x, t) dx \quad (15)$$

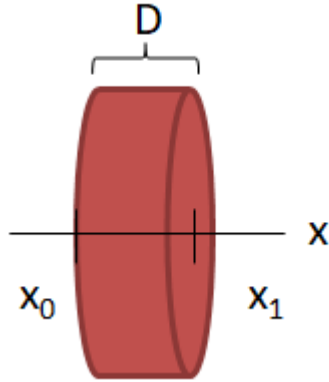


Figure 19: Section of bar

Differentiating using *Leibnitz* rule:

$$\frac{dH}{dt} = c\rho \int_{x_0}^{x_1} u_t(x, t) dx \quad (16)$$

Because of the assumption that the sides of the bar are insulated, the only way heat can flow into or out of D is through the ends at x_0 and x_1 . In 1822, Jean Baptiste Joseph Fourier described that heat flows from warmer regions to colder regions [55]. Furthermore the flow is proportional to u_x . The heat change H in D is now given by the heat flowing in D minus the heat leaving the section D (see equation (17)).

$$\frac{dH}{dt} = -\kappa u_x(x_0, t) - (-\kappa u_x(x_1, t)) \quad (17)$$

Equation (17) now describes a positive heat flow from left x_0 to right x_1 given by the sign. But this is only possible if the temperature at the left side is higher than the temperature at the right side.

This results in the connection:

$$\frac{dH}{dt} = \kappa u_x(x_1, t) - \kappa u_x(x_0, t) = \int_{x_0}^{x_1} \kappa u_{xx}(x, t) dx \quad (18)$$

Equating the two expressions for $\frac{dH}{dt}$ (equation (16) and equation (18)) the two expressions results in the connection:

$$c\rho \int_{x_0}^{x_1} u_t(x, t) dx = \kappa \int_{x_0}^{x_1} u_{xx}(x, t) dx \quad (19)$$

If we differentiate the left and right side with respect to x_1 , we get the heat equation in 1 dimension (equation (20)).

$$c\rho u_t = \kappa u_{xx} \Rightarrow u_t = \alpha u_{xx} \quad (20)$$

2.2.3 Numeric of partial differential equations

One problem with computers is that they can only handle algebraic equations. In order to solve partial differential equations, the requirement is to replace non algebraic expressions of these equations with corresponding algebraic expressions. One approach is to use *Finite Differences* to find algebraic expressions for partial differential equations [27]. The aim of this method is to find approximations for the function you are looking for, using discrete values of the independent variable. Due to the discrete approach to the exact solution, approximation errors arise that should not be ignored. Furthermore, the stability of the method used must be checked.

Derivation of finite differences based on the Taylor series

As already described above, the requirement is to replace derivatives of the differential equation with algebraic expressions [27]. To achieve this, the derivative for a function can be used (see equation)

$$f'(x) = \lim_{\Delta x \rightarrow 0} \frac{f(x + \Delta x) - f(x)}{\Delta x} \quad (21)$$

For small steps Δx , a good approximation solution for the differential quotient can now be achieved, see equation (22) which represents the forward differential quotient [22]. The error due to the approximation can be calculated using the *Taylor series*.

$$f'(x) \approx \frac{f(x + \Delta x) - f(x)}{\Delta x} \quad (22)$$

If one knows the function value at the position x , then the position $x + \Delta x$ and $x - \Delta x$ can be calculated with the help of the *Taylor series*. The Taylor series development of the position $x + \Delta x$ and $x - \Delta x$ describe formulas 1 and 2

$$f(x + \delta x) = f(x) + \frac{\Delta x}{1!} f'(x) + \frac{\Delta x^2}{2!} f''(x) + \dots \quad (23)$$

$$f(x - \delta x) = f(x) - \frac{\Delta x}{1!} f'(x) + \frac{\Delta x^2}{2!} f''(x) - \dots \quad (24)$$

By combining equation (22) and (23) we now obtain the following expression:

$$f'(x) = \frac{f(x + \Delta x) - f(x)}{\Delta x} - \frac{\Delta x}{2!} f''(x) - \frac{\Delta x^2}{3!} f'''(x) - \dots \quad (25)$$

If one chooses the increment Δx smaller than 1, the first summand is dominant over the rest. The rest is now a measure of the local error of the procedure. Equation (26) now describes the right-sided or forward difference quotient [22] with the error \mathcal{O} .

$$f'(x) = \frac{f(x + \Delta x) - f(x)}{\Delta x} + \mathcal{O}(\Delta x) \quad (26)$$

By using the Taylor series development according to formula 1 one obtains the rearward or left-side difference quotient [22] (see equation (27)).

$$f'(x) = \frac{f(x) - f(x - \Delta x)}{\Delta x} + \mathcal{O}(\Delta x) \quad (27)$$

Forming the difference between formulas 1 and 2 gives the central difference quotient. In equation (28) it can be seen that the error is reduced to $\mathcal{O}(\Delta x^2)$ in this formulation.

$$f'(x) = \frac{f(x + \Delta x) - f(x - \Delta x)}{2\Delta x} + \mathcal{O}(\Delta x^2) \quad (28)$$

If the differential equation requires the forming of the second derivative, this can be achieved by the addition of equation (23) and (24). The second derivative can now be seen in (29) with the error $\mathcal{O}(\Delta x^2)$.

$$f''(x) = \frac{f(x + \Delta x) - 2f(x) + f(x - \Delta x)}{\Delta x^2} + \mathcal{O}(\Delta x^2) \quad (29)$$

Looking now at the heat equation (see equation (20)), the partial derivative of the function $u = u(x, t)$ can be approximated either by the right-sided or forward difference quotient of equation (26), the rearward or left-side difference quotient (27) or the central difference quotient (28). However the term of the second partial derivative $u_{xx}(x, t)$ of the heat equation can be approximated with the central differential quotient as can be seen in equation (29).

2.3 Overview of most used Algorithms for Feature Extraction

In order to generate a single image from a sequence of thermograms, which includes all defects as well as inhomogeneities, is the aim of the following methods. Of course, each algorithm has its advantages and disadvantages. Some are more stable towards noise but are sensitive to inhomogeneous excitation. The aim of this work, however, is not to study the strengths and weaknesses of the following algorithms but to show which principles they use to map inhomogeneities in a single image and why we need them for further processing.

If defects and inhomogeneities have been imaged on a picture, further features can be extracted based on their now known localization.

2.3.1 Pulsed Phase Thermography (PPT)

Pulsed Phase Thermography (PPT) is one of the most commonly used algorithms for feature extraction [64] [81] [47]. The aim of this method is to split signals into sinus and cosine parts. So you can see that one transforms signals from the time domain into the frequency domain. So this method employs application on the *Fourier transformation*. The analogy of the discrete Fourier transformation is that the signal $x[n]$ is replaced by the thermograms $T(n(x, y))$, as seen in equation (30), where $T(x, y)$ describes the fourier coefficient at pixel (x, y) , n the frame increment, N the frames per period and k the frequency component.

$$T(x, y) = \sum_{n=0}^{N-1} T(n(x, y)) \exp^{-j \frac{2\pi n}{N} k} \quad (30)$$

If we look at equation (30) we are able to split this equation into a real part and an imaginary part, as seen in equation (31).

$$T(x, y) = \sum_{n=0}^{N-1} T(n(x, y)) \cdot \cos\left(\frac{2\pi n}{N} k\right) - \sum_{n=0}^{N-1} T(n(x, y)) \cdot j \cdot \sin\left(\frac{2\pi n}{N} k\right) \quad (31)$$

where:

$$S_0 = \sum_{n=0}^{N-1} T(n(x, y)) \cdot \sin\left(\frac{2\pi n}{N} k\right) \quad (32)$$

$$S_{90} = \sum_{n=0}^{N-1} T(n(x, y)) \cdot \cos\left(\frac{2\pi n}{N}k\right) \quad (33)$$

By the property of the orthogonality of (32) and (33) we are able to calculate an amplitude image (see equation (34)) and a phase image (see equation (35))

$$A = \sqrt{S_0^2 + S_{90}^2} \quad (34)$$

$$\phi = \arctan\left(\frac{S_{90}}{S_0}\right) \quad (35)$$

Figure 20 additionally shows a schematic representation of the calculation of the two components S_0 and S_{90} at one frequency component.

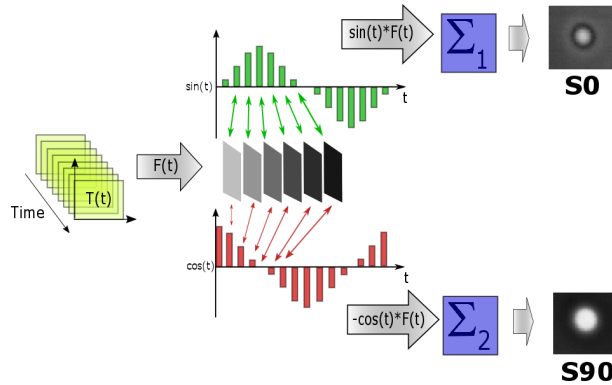


Figure 20: Schematic representation of PPT [23].

2.3.2 Wavelet Transformation

Wavelet transformation originates in geophysics in the early 1980s by Morlet et al and is a relative new technique which is used in data reduction, data compression and signal processing [52] [70]. Roughly speaking, the wavelet transformation can be seen as an improvement of the short-time fourier transformation (STFT) [37]. The principle of the wavelet transformation is that temporally localized waves or functions are used as a basis to achieve a time and frequency resolution. The improvement of the wavelet transformation compared to the STFT lies in the variable frequency resolution. The window function includes the frequency information and is by Wavelet transformation a modulated window function (**Wavelet = modulated window function**).

Figure 21 shows the window function for STFT and figure 22 the window function for Wavelet transformation.

It can be seen that a small window ends in a low frequency resolution as in opposite a wide window ends in a high frequency resolution. It is therefore not possible to achieve the best possible resolution simultaneously in the time domain and in the frequency domain.

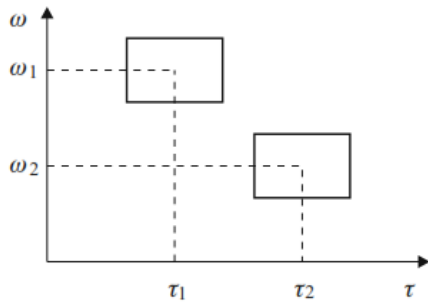


Figure 21: Frequency resolution of STFT

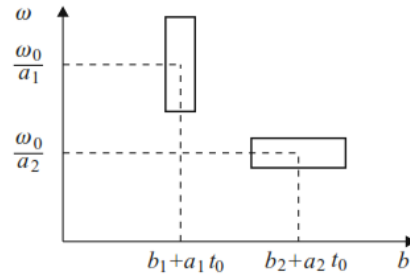


Figure 22: Frequency resolution of Wavelet transform

In the equation (36) you can see the definition of the continuous Wavelet transform of a signal $x(t) \in L_2(\mathbb{R})$ which results in $W_x(b, a)$ and is the inner product of the signal $x(t)$ with shifted and scaled version of the function $\Psi(t)$. To make sure that all of the functions $|a|^{-1/2}\Psi(t/a)$ for all $a \in \mathbb{R}^+$ have the same energy, factor $|a|^{-1/2}$ was introduced. Furthermore, the factor a can be used to elongate and compress a Wavelet. Thus, with the factor $a > 1$, the Wavelet can be stretched and the factor b translates the Wavelet at the time axis t .

$$W_x(b, a) = |a|^{-\frac{1}{2}} \int_{-\infty}^{\infty} x(t) \Psi\left(\frac{t-b}{a}\right) dt \quad (36)$$

Discrete Wavelet Transformation (DWT)

The discrete wavelet transformation was developed by Meyer and Mallat in the year 1988 which is based on a digital high- and low pass pair [65]. The basic concept of DWT is that the signal is decomposed into a rough inexact representation (low pass) and into a representation with exact details (high pass). These suitable high- and low passes cut the frequency region in half without losing information. Mallat and Meyer show following context that the continued (recursive) digital filtering of the low pass portion creates coefficient sets that correlate to a Wavelet transform. Figure 23 shows a

schematic representation of a level 2 decomposition. The maximal decomposition is limited by $\log_2(N)$ where N is the length of the signal [66].

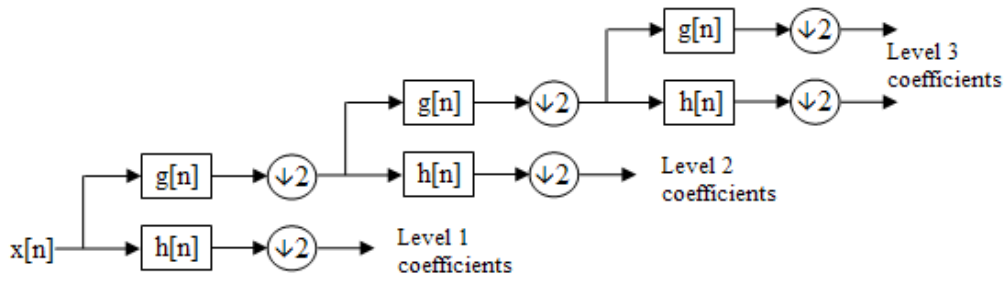


Figure 23: Schematic representation of DWT - Level 3 [3].

2.3.3 Principle Component Thermography (PCT)

Another common method to extract features from thermograms is *Principle Component Thermography*. PCT is based on *Singular value decomposition (SVD)* and is an eigenvector based transformation which forms an orthogonal space. The main goal of SVD is to extract spacial and temporal features from thermograms. To achieve this, the data matrix A must exist in the format $M \times N$ where $M > N$ [82].

A SVD of a matrix A of rank r is called a product of shape:

$$\mathbf{A} = \mathbf{U}\mathbf{S}\mathbf{V}^T \quad (37)$$

\mathbf{S} = is a diagonal $N \times N$ matrix which consists of singular values of \mathbf{A} in diagonal

\mathbf{U} = is a matrix in the form of $M \times N$

\mathbf{V}^T = is a $N \times N$ matrix

A schematic representation of SVD is shown in figure 24. To extract spatial variations of the data or better known as the *empirical orthogonal functions (EOF)* the columns of the matrix \mathbf{U} are used. To get the time variation of the data matrix, known as the *principle components (PC)*, the rows of the matrix \mathbf{V}^T are used [82].

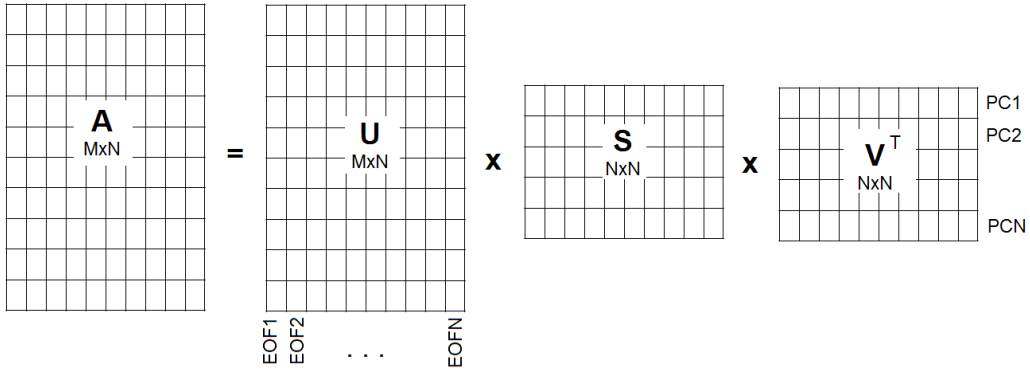


Figure 24: Schematic representation of SVD

As described above, the technique of SVD is used to extract spatial EOFs and temporal PCs [82] [86]. To extract features using PCT, first the 3D thermograms must be converted into a 2D matrix whereby time is represented along the columns and space in a row vector. To apply PCT to thermograms, the data must first be standardized. This can be done by equation (38)

$$\hat{A} = \frac{A - A_{mean}}{std(A)} \quad (38)$$

There are two types to calculate A_{mean} . Either the mean image is subtracted from each figure (39) or the temporal mean is subtracted from each temporal profile (40).

$$\mu_M = \frac{1}{N} \sum_{n=1}^N A(n, m) \quad (39)$$

$$\mu_N = \frac{1}{M} \sum_{m=1}^M A(n, m) \quad (40)$$

2.3.4 Statistical parameters

Another technique in signal processing to describe non-linear signals is to look at the characteristics of the distribution of a random variable. The following section briefly describes how it can be deduced to such characteristics, called cumulants [58].

The *Cumulative Distribution Function (CDF)*, as can be seen in figure 25, represents that the random variable X takes on a value less than or equal to ξ .

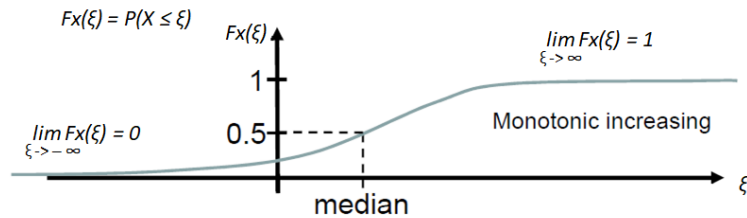


Figure 25: Cumulative distribution function CDF of a random variable X [58]

The *Probability Density Function (PDF)* can be deduced from the CDF as the derivative of the CDF (see figure 26). A requirement is that the PDF has to be continuous and differentiable.

Now we assume that we add two random variables. This leads to the final PDF being the convolution of the two single PDFs of the two random variables (see equation (41)).

$$f_{X+Y}(\xi) = f_X(\xi) * f_Y(\xi) \quad (41)$$

Applying the *Fourier transformation* to equation (41) results in:

$$\Phi_{X+Y}(\mu) = \Phi_X(\mu)\Phi_Y(\mu) \quad (42)$$

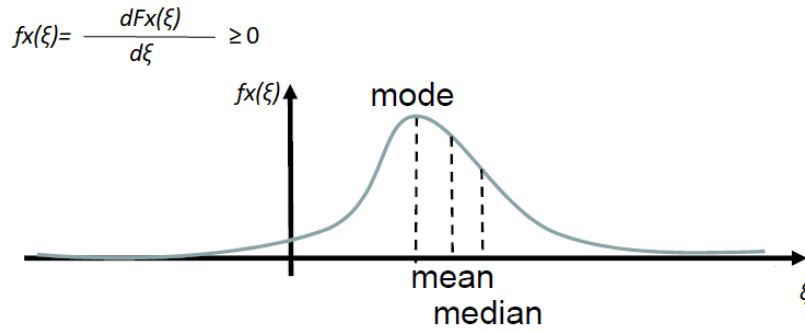


Figure 26: Probability density function PDF of a random variable X [58]

If we now apply the natural logarithm to equation (42) we receive:

$$\ln\Phi_{X+Y}(\mu) = \ln\Phi_X(\mu) + \ln\Phi_Y(\mu) \quad (43)$$

Finally to get the cumulant-generating function, the function $\ln\Phi_X(\mu)$ at $\mu = 0$ has to be approximated with *Taylor series* like in the equation

$$\ln\Phi_X(\mu) = \sum_{p=0}^{\infty} \frac{1}{p!} c_{X,p} \mu^p \quad (44)$$

Now we are able to generate cumulants from the cumulant generating function (44). An overview of the first four cumulants is given in table 3.

Table 3: Overview of cumulants

Cumulant	Name
c1	mean
c2	variance
c3	skewness
c4	kurtosis

2.4 Related work on depth estimation

The methods mentioned in the previous chapter are used to find inhomogeneities in the specimen. It is not only important to find inhomogeneities but also to characterize them. The depth of inhomogeneities is one of the important features that often need to be extracted [97]. To achieve this, most methods introduce a characteristic time that is proportional to the depth of the inhomogeneity. To get this characteristic time usually one or more reference points from the sound area are needed [97] [60]. Simply explained, as already mentioned, the surface of a specimen heats up during active thermography. After excitation of the surface of the specimen, the heat spreads in the specimen and thereby causes a continuous decrease of the surface temperature. If inhomogeneities with a higher thermal resistance are present in the test specimen, they cause a delay in heat dissipation. This results in a higher temperature at inhomogeneity points compared to surface area. If inhomogeneities near the surface, these temperature differences will occur earlier. If inhomogeneities are deeper inside the specimen the temperature differences will occur later.

These temperature differences result in a temperature contrast of.

$$\Delta = T - T_R \quad (45)$$

Figure 27 schematically shows the above described principle of active thermography and figure 28 shows a practical example.

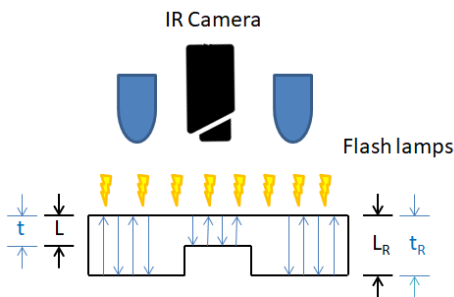


Figure 27: Schematic principle of active thermography

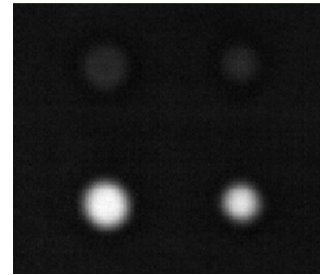


Figure 28: Practical example of active thermography

2.4.1 Log Second Derivative (LSD)

In the subsection above, it has already been roughly outlined that there are preconditions for determining the depth of inhomogeneities. The first

requirement necessary for all algorithms is the knowledge of the thermal diffusivity α [93]. This means that the correct material constant α must first be found using the method described in section 4.7. In order to determine the depth, the characteristic time has to be extracted. The first method to extract the characteristic time is the *Log Second Derivative (LSD)* [31]. With this method, each pixel of the thermographic sequence is first scaled into the log-log space and approximated using polynomial fit. The exact method is called *Thermographic Signal reconstruction (TSR)* [85] and is described in chapter 4.5. The second derivative is then calculated from the approximated signals.

Parker et. al. defined the decay of the surface temperature T of the one dimensional heat equation with time t as:

$$T(t) = \frac{Q}{\rho CL} \left[1 + 2 \sum_{n=1}^{\infty} \exp\left(-\frac{n^2 \pi^2}{L^2} \alpha t\right) \right] \quad (46)$$

Q = input energy
 ρ = density
 C = specific heat
 α = thermal diffusivity
 L = sample thickness

By computing the second derivative of equation (46) and extracting the time of the maximum peak the depth of the inhomogeneity is estimated by equation (??).

$$L = \sqrt{\pi \cdot \alpha \cdot t_{peak}} \quad (47)$$

2.4.2 Absolute Peak Slope Time (APST)

The huge advantage of the next method APST is that no reference point is needed to determine the depth of inhomogeneities. This method was invented by Zeng et. al. [98]. His paper describes the linear connection between the square of the depth of inhomogeneities and the absolute peak slope time t_{APST} .

Zeng et. al. [98] also described an equation for the case that inhomogeneities are inside a specimen:

$$\Delta T(t) = \frac{Q}{e\sqrt{\pi t}} \left[1 + 2 \sum_{n=1}^{\infty} \exp\left(-\frac{n^2 L^2}{\alpha t}\right) \right] \quad (48)$$

Q = input energy
 α = thermal diffusivity
 L = defect depth
 e = thermal effusivity

Next both sides of equation (48) are multiplied by the square root of the time \sqrt{t} . Multiplying \sqrt{t} produces a new time dependent function f , as can be seen in equation (49).

$$f(t) = \Delta T(t) \cdot \sqrt{t} = \frac{Q}{e\sqrt{\pi}} \left[1 + 2 \sum_{n=1}^{\infty} \exp\left(-\frac{n^2 L^2}{\alpha t}\right) \right] \quad (49)$$

The next step is to estimate the first derivative of equation (49), which results into:

$$f'(t) = \frac{2Q}{e\sqrt{\pi}} \sum_{n=1}^{\infty} \exp\left(-\frac{n^2 L^2}{\alpha t}\right) \cdot \frac{n^2 L^2}{\alpha t^2} \quad (50)$$

Now we have to find the absolute peaks. Therefore, we calculate the second derivative of equation (50) and find the roots. The second derivative is given in equation (51).

$$f''(t) = \frac{2Q}{e\sqrt{\pi}} \sum_{n=1}^{\infty} \exp\left(-\frac{n^2 L^2}{\alpha t}\right) \cdot \frac{n^2 L^2}{\alpha t^3} \cdot \left(\frac{n^2 L^2}{\alpha t} - 2\right) \quad (51)$$

Finally the *absolute peak slope time* t_{APST} can be estimated by:

$$t_{APST} = \frac{L^2}{2\alpha} \quad (52)$$

and the depth of the inhomogeneity can thus be calculated by equation (53).

$$L = \sqrt{2 \cdot \alpha \cdot t_{APST}} \quad (53)$$

3 Preprocessing Techniques

3.1 Fixed Pattern Noise (FPN)

The reason why FPN occurs is primarily due to production-related tolerances. These tolerances cause a deviation by a fixed offset in the image, but can be corrected by a correction (addition or multiplication) per pixel [99]. In order to determine the correction factor, the FPN is measured without light. By measuring without light, the FPN is also often referred to as *Dark Signal Non Uniformity (DSNU)* [88].

Ideally, each pixel should have the same value if uniform light falls on the camera sensor. However, small deviations in the production of the sensor cells lead to slight differences in the pixels. These deviations of the pixels are referred to as *Photo Response Non Uniformity (PRNU)* [96] in the camera technique. Due to the physical tolerances of the production, the PRNU cannot be finally corrected.

3.2 Bad Pixel

Bad Pixels can occur in the camera sensor in two ways. Either such bad pixels always appear as dark ones, then one speaks of *dead pixels*. Or they appear as white pixels in the picture, then one speaks of *stuck pixel*. When it comes to high-quality cameras, these pixels are detected by the camera's firmware and repaired by themselves. The defective pixel is then ignored during acquisition and then an average value is calculated. In order for the firmware to detect such *Bad Pixel*, a corresponding list of defective pixels must be available. In general, the camera sensor is tested after production on bad pixels and the list of bad pixels is firmly programmed. If bad pixels occur after production due to aging or environmental influences, they are not recognized by the firmware and must be removed afterwards [20].

3.3 Signal fitting

If signal fitting is used in numerical mathematics, there are essentially two different types: *Interpolation* and *Approximation*.

Interpolation

When it comes to interpolation, a function needs to be found for known points (for example results of a measurement) that describes these points and connects them by a curve. If interpolation is used, it is essential that the

given data points describe the measurement as exactly as possibly (noise free observation). Simplified, it can be said that for a given list of input/output sample pairs (x_i, y_i) we have to find an interpolation function $\hat{f}(x_i)$ such as:

$$\hat{f}(x_i) = y(i) \quad \forall pairs(x_i, y_i) \quad (54)$$

and meet additional constraints such as

- Smoothness
- Band limitedness
- Piecewise constant

The most used interpolation methods are: Linear Interpolation, Higher-Order Polynomials, Cubic Spline Interpolation, Sinc Interpolation and Lagrange Interpolation. Due to the given measurement noise of the IR-camera, interpolation is only of minor importance in this thesis [58].

Approximation

To extract depths of thermogram sequences temporal noise-free cooling processes are needed. Approximation is a method that is more stable compared to noisy measurement results. It aims at representing given observations by a simpler function. In general, approximation has certain advantages over interpolation as for example: proper handling of noisy measurement or flexible trade-off between model complexity and model accuracy.

In other words, the method approximation should find a function $\hat{f}(x_i)$, for a given list of input/output sample pairs (x_i, y_i) which can be corrupted by noise. This minimizes a cost function or approximation measures and meet additional constraints such as

- Smoothness
- Band limitedness
- Piecewise constant

Cost functions or approximation measures can exist as:

- L-Norm: $\int_D |f(x) - \hat{F}_P(x)|^L < \epsilon$
- Least squares (L=2): $\int_D |f(x) - \hat{F}_P(x)|^2 dx < \epsilon$
- Chebyshev or uniform approximation: $(L \rightarrow inf) sup|f(x) - \hat{f}_P(x)| < \epsilon$

The most widely used approximation methods that are applicable are Polynomial Approximation, Fourier Series, Radial Basis Functions or Multi-layer Perceptrons Neuron [58].

In this thesis, we use *Least squares polynomial fit*, as can be seen in equation (55), which fits a polynomial of degree n to points (x, y) . This solution minimizes the squared error $E = \sum_{j=0}^k |p(x_j) - y_j|^2$.

$$p(x) = p_0 + p_1x^n + p_2x^{n-1} + \dots + p_nx + p_{n+1} \quad (55)$$

Now, if one has decided to approximate data with polynomial fit then the question of the degree of the polynomial arises. If you increase the order of the polynomial, the sum of the squares of the residuals $\sum_{i=1}^N |\epsilon_i^2|$ will always be smaller until 0 is reached, in case the polynomial order is chosen is one less than the number of data points. This achieves an exact replica of the data. To avoid overfitting the sum of the squares of the residuals will be weighted, as can be seen in equation (56). The order of the polynomial is now chosen so that equation (56) reaches a minimum or there is no significant decrease in its value as the degree of polynomials is increased [4].

$$\frac{\sum_{i=1}^N |\epsilon_i^2|}{N - n - 1} \quad (56)$$

N = Number of data points
 n = order of polynomial
 ϵ = Residuals

4 Processing Techniques

4.1 Thermographic Signal Reconstruction (TSR)

In active thermography, TSR is a popular and attractive method of data processing to increase the quality of thermographic images. By reducing temporal noise, TSR can improve both temporal and spatial image resolution as well as dramatically improve the signal-to-noise ratio (SNR) of a given pixel as well. The result is a temporal low-pass filtered thermography signal without additional noise [85].

In order to counteract the inhomogeneous temperature distribution of the

sample before excitation, the cooling process is subtracted from each pixel with a reference image before the excitation. By forming the logarithm of the cooling process and its time, the exponential curve becomes a linear function. By forming a polynomial fit, the SNR is subsequently improved. Advantage of a polynomial fit is certainly the broad range of functions that can very flexible be fit.

In general, TSR is based on polynomial fit. The goal is to fit the logarithmic time dependence of thermographic signals with an n-order polynomial function, as can be seen in equation (57).

$$\ln(T - T_0) = p_0 + p_1 \ln(t) + p_2 [\ln(t)]^2 + \dots + a_n [\ln(t)]^n \quad (57)$$

The improved SNR of the thermographic signals is an advantage. Another great advantage of this method is that now derivatives of the signals can be calculated. The derivation of thermographic signals allows differences in the cooling behavior to be seen more easily. It is also possible to calculate the characteristic time for depth determination by derivations of the signals. An important factor of this method is the correct determination of the degree of the polynomial. If the polynomial is too small or too large, important features are either filtered out or an overfitting of the signals is caused [4]. In figure 29, an original thermographic signal whereas in figure 30, the TSR-signal of the original signal can be seen.

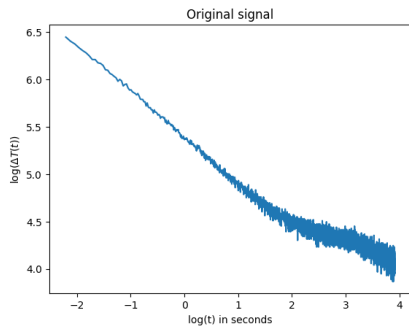


Figure 29: Original thermographic signal in logarithmic scale

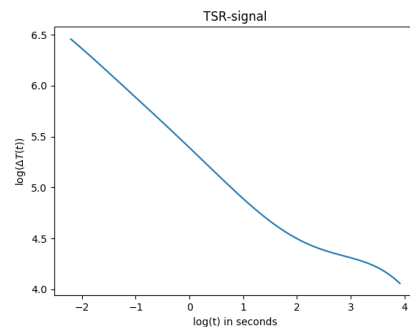


Figure 30: TSR-signal in logarithmic scale

4.2 Contrast Methods

Active thermography uses an external excitation source to induce energy into the material. As already described, in case of inhomogeneities, the thermal

resistance is either greater or less than the background, and thus provides a thermal contrast whereby features can be extracted [84]. However, this assumption is only correct if the energy of the excitation source excites the specimen uniformly. In reality, excitation sources have a non-uniform illumination, as can be seen in figure 31, causing the specimen to be excited differently. This difference may cause the thermal contrast between inhomogeneity and background to be lost.

The following methods are different methods to compensate the non-uniform heating. In figure 32, a compensated thermogram can be seen.

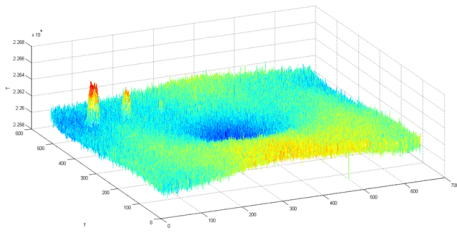


Figure 31: Thermogram of a non-uniform excited specimen

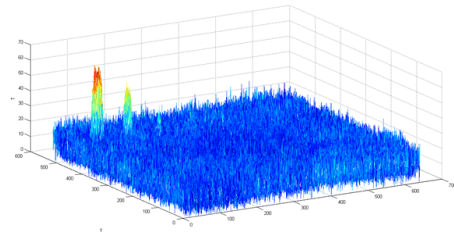


Figure 32: Thermogram of a compensated non-uniform excitation

4.2.1 Absolute Contrast

The first and easiest way to compensate non-uniform heating is the procedure Absolute Contrast. In this case, it is necessary to select one or more points which have a specific cooling characteristic at the specimen [49]. The signal or mean of the signals is then subtracted from each point as can be seen in equation (58).

$$AbsCtrst_{(x,y)}(t) = T_{(x,y)}(t) - T_{snd}(t) \quad 0 \dots if \quad AbsCtrst(x,y) < 0 \quad (58)$$

4.2.2 Running Contrast

The next method, Running Contrast, is a method very similar to the Absolute Contrast method. Here again one or more points must be selected, which are characteristic for the cooling process. Again the selected background is subtracted from each pixel but then scaled to T_{snd} [17], as can be seen in equation (59).

$$RunCtrst_{(x,y)}(t) = \frac{T_{(x,y)}(t) - T_{snd}(t)}{T_{snd}(t)} \quad 0 \dots if \quad RunCtrst(x,y) < 0 \quad (59)$$

4.2.3 Normalized Contrast A

The normalized contrast method is one of two similar methods. With this method, one or more reference points must be selected just as in the previous two methods. The principle of this procedure is that each pixel of each thermogram is scaled to its final temperature value and also the selected reference signal is scaled to its final temperature value. Then, each pixel of the scaled thermogram is subtracted with the scaled reference signal [17] (see equation (60)).

$$NormCtstA_{(x,y)}(t) = \frac{T_{(x,y)}(t)}{T_{end}(x,y)} - \frac{T_{snd}(t)}{T_{snd_end}} \quad (60)$$

4.2.4 Normalized Contrast B

The difference of this method compared to the first normalized contrast method is that the scaling factor is not the final temperature but the starting temperature after the excitation [17]. The calculation method of this method is described in formula (61).

$$NormCtstB_{(x,y)}(t) = \frac{T_{(x,y)}(t)}{T_{start}(x,y)} - \frac{T_{snd}(t)}{T_{snd_start}} \quad (61)$$

4.2.5 Standard Contrast

In the standard contrast method, the self-heat before the excitation is included in the calculation. Again, one or more reference points must be chosen. Each thermogram after the excitation is subtracted with the thermogram before the excitation and also the reference point is subtracted with the reference point before the excitation. Thereafter, the individual thermograms are scaled with the corrected reference point [62] (see equation (62)).

$$stdCtst_{(x,y)}(t) = \frac{T_{(x,y)}(t) - T_{preflash}(x,y)}{T_{snd(x,y)}(t) - T_{snd_preflash}} \quad (62)$$

4.2.6 Differentiated Absolute Contrast (DAC)

In the last contrast DAC we assume that at time $t = 0$, the heat pulse is applied to the specimen. At this time, the recording of the thermograms begins and lasts until the time t_f . If a heat pulse hits the specimen, it takes a while for the heat pulse to spread and the first defect to occur. The time

that is assumed until the first defect occurs is referred to as t' [30]. In this case, equation (63) will be the result.

$$T_{s(x,y)}(t') = T_{x,y}(t') \quad (63)$$

We now assume a semi-infinite body to which a Dirac pulse is applied. Under these circumstances the 1-dimensional Fourier equation is solved as:

$$\Delta T_{semi_infinite_body}(z = 0, t) = \frac{Q}{e\sqrt{\pi t}} \quad (64)$$

z = Depth
 Q = Injected Energy
 e = Thermal effusivity
 ΔT = Temperature increase from $t=0$

With assumption (63) the sound area $T_{s(x,y)}(t')$ is given by:

$$\Delta T_{s(x,y)}(t') = \Delta T_{(x,y)}(t') = \frac{Q_{(x,y)}}{e_{(x,y)}\sqrt{\pi t'}} \quad (65)$$

Now we can extract the ratio of the unknown parameters Q/e as:

$$\frac{Q_{(x,y)}}{e_{(x,y)}} = \sqrt{\pi t'} \cdot \Delta T_{(x,y)}(t') \quad (66)$$

Equation (67) now describes the temperature of the sound area as function of time t .

$$\Delta T_{s(x,y)}(t) = \frac{Q_{(x,y)}}{e_{(x,y)}\sqrt{\pi t}} = \frac{\sqrt{\pi t'}}{\sqrt{\pi t}} \cdot \Delta T_{(x,y)}(t') = \sqrt{\frac{t'}{t}} \cdot \Delta T_{(x,y)}(t') \quad (67)$$

Finally, DAC is defined as can be seen in equation (68).

$$DAC_{(x,y)}(t) = \Delta T_{(x,y)}(t) - \sqrt{\frac{t'}{t}} \cdot \Delta T_{(x,y)}(t') \quad (68)$$

4.3 Determination of the thermal diffusivity α

An important point of this thesis is the determination of the depth of inhomogeneities in the specimen. If one has information about the characteristic time, additional information of the material property of the specimen is needed to determine the depth of inhomogeneities. This required material

property is the thermal diffusivity α , which describes the temporal change of the spatial distribution of the temperature. The thermal diffusivity α is defined as:

$$\alpha = \frac{\lambda}{\rho \cdot c} \quad (69)$$

λ = Thermal conductivity

ρ = Density

c = Specific heat capacity

In order to determine the thermal diffusivity the principle of Parker et al. [93] is adopted. In general, a test object is heated at one side and at the opposite side the increase of the temperature is measured. The increase of the temperature is then proportional to the thermal diffusivity α . In equation (70), the formula to determine the thermal diffusivity α is displayed.

$$\alpha = \frac{1.38 \cdot L^2}{\pi^2 t_{1/2}} \quad (70)$$

$t_{1/2}$ = time required for the back surface to reach half of T_{max}

L = Thickness of the specimen

e = Thermal effusivity

The exact derivation of the formula would go beyond the scope of this thesis, but can be read in Parker's et. al. paper [93].

4.4 Implementation of heat equation

4.4.1 Explicit procedure

In this chapter, various methods are shown for the numerical solution of the heat equation. In order to solve the heat equation, a suitable initial- and/or boundary condition is needed. Now let us assume a thin rod whose length is given by $0 \leq x \leq 1$. Thus, the initial condition is given by formula (71), where $g(x)$ is a given function [44].

$$u(x, 0) = g(x) \quad \text{for } x \in [0, 1] \quad (71)$$

The boundary conditions with constants a and b are given by equation (72).

$$u(0, t) = a, \quad u(1, t) = b, \quad t \leq 0 \quad (72)$$

With the heat equation, the given initial condition and the boundary conditions, the model of a thin rod, whose ends are kept at the constant temperatures a and b , is given. The solution $u_t(x, t) = u_{xx}(x, t)$ then delivers the temperature distribution within the rod as a function of time.

As already described in chapter 2.2.3, derivatives must be replaced by approximations. This is done by using finite differences. Thus, the length of the rod as well as the time is covered with a grid of lattice points. In other words, the length of the rod as well as the temporal change is subdivided into equally long subintervals. The grid points are now defined as (x_j, t_m) , where the temporal changes are given as $t_m = m\Delta t$ and the length intervals are given as $x_j = j\Delta x$. The solution u_j^m is now the approximated solution at the grid point (x, t) [44].

In the explicit solution method, the partial derivative of the function $u = u(x, t)$ according to the time variable t is approximated by the forward differential quotient, as outlined in equation (73).

$$u_t(x_j, t_m) \approx \frac{u_j^{m+1} - u_j^m}{\Delta t} \quad (73)$$

The second partial derivative $u_{xx}(x, t)$ is approximated by the central differential quotient [27], as depicted in equation.

$$\Delta u(x_j, t_m) \approx \frac{u_{j+1}^m - 2u_j^m + u_{j-1}^m}{(\Delta x)^2} \quad (74)$$

If the heat equation with equation (73) is replaced by and equation (74), we get the approximated solution in direction forward (see)

$$\frac{u_j^{m+1} - u_j^m}{\Delta t} = \alpha \frac{u_{j+1}^m - 2u_j^m + u_{j-1}^m}{(\Delta x)^2} \quad (75)$$

The equivalent of equation (75) is :

$$u_j^{m+1} = u_j^m + \mu(u_{j+1}^m - 2u_j^m + u_{j-1}^m) \quad (76)$$

where

$$\mu = \frac{\alpha \Delta t}{(\Delta x)^2} \quad (77)$$

In A it is shown that condition (78) must be fulfilled in order to ensure the stability of this procedure [39].

$$\Delta t \leq \frac{(\Delta x)^2}{2\alpha} \quad (78)$$

By approximating the heat equation with finite differences, a residual amount e is given, which indicates the error of the approximation. The error e is also called the local discretization error and can be estimated as a function of Δt and Δx .

Thus, for the implicit method there is a discretization error which is of first order with respect to the time and second order with respect to the location (see equation (79)). For more details see [44].

$$e = \mathcal{O}(\Delta t) + \mathcal{O}((\Delta x)^2) \quad (79)$$

4.4.2 Implicit procedure

The implicit method has the advantage that the stability of this method is *unconditional*. This means that for every ratio for Δt and Δx , the stability is given. Looking now at the equation (80) of the implicit procedure, it is evident that the equation is similar to the equation of the explicit procedure (75). The difference is that the term u_j^m is replaced by the term u_j^{m+1} . Since the values of the terms u_{j+1}^{m+1} are all unknown, a system of equations is needed that implicitly contains the values [44].

$$\frac{u_j^{m+1} - u_j^m}{\Delta t} = \alpha \frac{u_{j+1}^{m+1} - 2u_j^{m+1} + u_{j-1}^{m+1}}{(\Delta x)^2} \quad (80)$$

We set as before:

$$\mu = \frac{\alpha \Delta t}{(\Delta x)^2} \quad (81)$$

and we are able to write equation (80) as:

$$(1 + 2\mu)u_j^{m+1} - \mu(u_{j+1}^{m+1} + u_{j-1}^{m+1}) = u_j^m, \quad j = 1, \dots, n \quad (82)$$

Concerning the implicit procedure, it is necessary to solve a linear equation system with each step to get u_j^{m+1} from u_j^m . The linear equation system can be seen in equation.

$$(I + \mu A)u^{m+1} = u^m + b, \quad m = 0, 1, \dots \quad (83)$$

The tridiagonal matrix A is given as:

$$\left(\begin{array}{cccccccc} 2 & -1 & & & & & & \\ -1 & 2 & -1 & & & & & \\ & & \cdot & \cdot & \cdot & & & \\ & & & \cdot & \cdot & \cdot & & \\ & & & & \cdot & \cdot & \cdot & \\ & & & & & -1 & 2 & -1 \\ & & & & & & -1 & -2 \\ & & & & & & & -1 \end{array} \right) \quad (84)$$

The vector b represents the boundary conditions and consists of zeros except for the first and last component which is $b_0 = \mu a$ and $b_{n+1} = \mu b$. As in the explicit method, there exists also a discretization error e in the implicit method. By approximating the heat equation with Δx and Δt , we get the same discretization error as in the explicit method (see equation 79) but with the big advantage of stability of the method.

4.4.3 Cranck-Nicolson procedure

The Cranck-Nicolson procedure is a stable procedure second order. It is a means between explicit and implicit method and the terms u_j^m and u_j^{m+1} are replaced by the arithmetic mean (see equation (85)) [44].

$$u_j^{m+\frac{1}{2}} = \frac{1}{2}(u_j^{m+1} + u_j^m) \quad (85)$$

By replacing with the arithmetic mean, the Cranck-Nicolson procedure is given by equation (86)

$$u_j^{m+1} - u_j^m = \frac{\alpha \Delta t}{2(\Delta x)^2} (u_{j+1}^{m+1} - 2u_j^{m+1} + u_{j-1}^{m+1} + u_{j+1}^m - 2u_j^m + u_{j-1}^m) \quad (86)$$

Again, this method can be specified in matrix vector form, as seen in formula (87).

$$(I + \frac{\mu}{2}A)u^{m+1} = (I + \frac{\mu}{2}A)u^m + b, \quad m = 0, 1, \dots \quad (87)$$

4.4.4 2-dimensional heat equation

2D-Explicit procedure

In equation (88), the heat equation can be seen in two space dimensions.

$$u_t(t, x, y) = \alpha(u_{xx}(x, y, t) + u_{yy}(x, y, t)) \quad (x, y) \in \Omega = (0, 1)^2 \quad (88)$$

Ω represents a flat plate with the edge $\delta\Omega$. As a boundary condition, we assume the temperature distribution on the four sides as displayed in equation (89) where g is a given function [44].

$$u(t, x, y) = g(x, y) \quad \text{for } (x, y) \in \delta\Omega \quad (89)$$

The initial condition is a function in the two space dimensions:

$$u(x, y, 0) = f(x, y) \quad \text{for } (x, y) \in \Omega \quad (90)$$

Similar to the one-dimensional case, a network of grid points is placed over the two-dimensional space of the plate. The central differences are approximated through equation (92) and equation (93) where h is the distance between horizontal and vertical direction.

For the crank nicolson method, a discretization error is eventuated, which is of second order with respect to time and is also of second order with respect to the location [44], as can be seen in equation (91).

$$e = \mathcal{O}((\Delta t)^2) + \mathcal{O}((\Delta x)^2) \quad (91)$$

$$u_{xx}(x_i, y_j, t) \approx \frac{u(x_{i-1}, y_j, t) - 2u(x_i, y_i, t) + u(x_{i+1}, y_j, t)}{h^2} \quad (92)$$

$$u_{yy}(x_i, y_j, t) \approx \frac{u(x_i, y_{j-1}, t) - 2u(x_i, y_i, t) + u(x_i, y_{j+1}, t)}{h^2} \quad (93)$$

The time derivation is then given as:

$$u_t(x_i, y_j, t_m) \approx \frac{u_{i,j}^{m+1} - u_{i,j}^m}{\Delta t} \quad (94)$$

This results in the equation:

$$\frac{u_{i,j}^{m+1} - u_{i,j}^m}{\Delta t} = \alpha \frac{u_{i-1,j}^m + u_{i+1,j}^m + u_{i,j-1}^m + u_{i,j}^m + 1 - 4u_{i,j}^m}{h^2} \quad (95)$$

Finally, equation (96) shows the explicit procedure for the two dimensional case.

$$u_{i,j}^{m+1} = u_{i,j}^m + \frac{\alpha \Delta t}{h^2} (u_{i-1,j}^m + u_{i+1,j}^m + u_{i,j-1}^m + u_{i,j}^m + 1 - 4u_{i,j}^m) \quad (96)$$

As already shown in the one-dimensional case, the explicit procedure has a stability condition [39]. Equation (97) shows that at small h , very small time steps are needed.

$$\Delta t \leq \frac{h^2}{4c} \quad (97)$$

2D-Implicit procedure

Not only the explicit method can be extended into the two-dimensional space but also the implicit procedure. The advantage of the implicit method is again, as in the one-dimensional case, that it is a stable method [27]. Analogously to the one-dimensional method, the values $u_{i,j}^m$ are replaced by $u_{i,j}^{m+1}$, resulting in equation (99).

$$\frac{u_{i,j}^{m+1} - u_{i,j}^m}{\Delta t} = \alpha \frac{u_{i-1,j}^{m+1} + u_{i+1,j}^{m+1} + u_{i,j-1}^{m+1} + u_{i,j+1}^{m+1} - 4u_{i,j}^{m+1}}{h^2} \quad (98)$$

By transforming formula 1, one obtains the calculation of the heat equation with the implicit method in the two-dimensional case seen in the equation below. The drawback of the two-dimensional implicit method is that every time step requires the solution of a two-dimensional Poisson equation [39].

$$u_{i,j}^{m+1} = u_{i,j}^m + \frac{\alpha \Delta t}{h^2} (u_{i-1,j}^{m+1} + u_{i+1,j}^{m+1} + u_{i,j-1}^{m+1} + u_{i,j+1}^{m+1} - 4u_{i,j}^{m+1}) \quad (99)$$

4.4.5 Determination of the initial condition

To calculate the initial condition we assume a semi-infinite body with transient conduction [24].

The solution of such a body with a heat flux at the surface $\dot{q}'' = -k \frac{\delta T}{\delta X} |_{x=0}$ can be seen in equation (71).

$$\Delta T = \frac{\dot{q}''}{k} \left[\sqrt{\frac{4\alpha t}{\pi}} \exp\left(-\frac{x^2}{4\alpha t}\right) - x \operatorname{erfc}\left(\frac{x}{\sqrt{4\alpha t}}\right) \right] \quad (100)$$

In order to calculate the initial condition, we set the position of the surface $x = 0$ and define the unknown scaling factor $\frac{\dot{q}''}{k}$ to s . Equation (71) results in:

$$\Delta T = s \left[\sqrt{\frac{4\alpha t}{\pi}} \exp(0) - 0 \right] = s \sqrt{\frac{4\alpha t}{\pi}} \quad (101)$$

Next, we calculate the first derivative of equation (101) and extract the unknown scaling factor s :

$$\frac{\delta \Delta T}{\delta t} 0 \frac{\alpha \cdot s}{\sqrt{\pi} \cdot \sqrt{\alpha t}} \Rightarrow s = \frac{\Delta T' \sqrt{\pi \alpha t}}{\alpha} \quad (102)$$

In order to calculate the time relative to the surface disturbance t , we start from equation (103).

$$\Delta T = \frac{\Delta T' \sqrt{\pi \alpha t}}{\alpha} \sqrt{\frac{4 \alpha t}{\pi}} \quad (103)$$

If we transform equation (103), it ends in:

$$t = \left(\frac{\Delta T \alpha}{\Delta T'} \right)^2 \cdot \frac{1}{4 \alpha} \quad (104)$$

4.4.6 Boundary conditions

As shown in the above-defined various types of implementation of the heat equation, the boundaries of the object to be simulated must be predetermined. Since this knowledge about the boundaries is often uncertain, this problem is called boundary problem. There are several approaches to solve this problem. Two widely used approaches takes up in this thesis are **Dirichlet Boundary conditions** [27] and **Neumann Boundary conditions** [27]. If a defined function is specified for the boundaries, this is called **Dirichlet Boundary conditions**.

If no function values, but derivation values for the boundaries are defined, these are called **Neumann Boundary conditions**.

4.5 Depth determination with new approach

4.5.1 Maximum Contrast

When considering the development of a method that simultaneously eliminates the influence of inhomogeneous illumination, a method was developed using the combination of heat equation and TSR.

Through the necessary input parameter thermal diffusivity α , which is needed to determine the exact depth of inhomogeneities, the heat equation with finite differences was simulated. If the parameter α was determined exactly for the specimen to be examined, we achieve the cooling process of an ideally homogeneous specimen without inhomogeneities. If the acquisition of the active thermography is subtracted from the simulation, ideally only inhomogeneities and detector noise are present in the acquisition sequence.

In order to eliminate the existing detector noise, each pixel is approximated using the TSR method [85], independent of the simulation of the heat equation. Thus, we have an ideal cooling process of a sample on the one hand and on the other hand a noise-free approximation of the real cooling process of each pixel.

By subtracting the heat simulation and the TSR approximation, the value in the background is now ideally 0. If there are inhomogeneities in the specimen, deviations occur due to the subtraction. Depending on whether inhomogeneities are introduced near the surface or in the depth, deviations will arise sooner or later.

Extracting the time of maximum deviation, the depth of inhomogeneity can be determined by equation (105).

$$L = \sqrt{t_{maxCtrst} \cdot \alpha} \quad (105)$$

5 Experiment Setup

5.1 Used IR-camera

All the results shown in this work were created using the infrared camera *IR 8300 hp* from Infratec. Table 4 gives an overview about the most important technical specifications of the IR-camera.

Table 4: Specification of *IR 8300 hp*

Infratec IR 8300 hp	
Detector Format (IR Pixels)	640 x 512
Detector	Cooled Indium-antimonide (InSb) - Focal Plane Array
Spectral range	MWIR, (2.0 - 5.7) μm
Detector cooling	Integrated, robust Stirling-Rotation cooler
Pixel size	15 μm
Temperature measuring range	NETD @30C <25mK, typical 20mK
Integration time	(1-20.000)us in 1 μs steps
Dynamic range	14 bit
Frame rate	Up to 300Hz

5.2 Used Flash lamp/Power supply

As excitation source a flash lamp from *Hensel* with the correlated power supply *TRIA 6000S* was used. Table 5 and table 6 again show the most important technical specifications.

Table 5: Specification of flash lamp

Hensel flash lamp	
Maximal Power	Up to 6000J
Modeling Light	Up to 650W
Cooling Fan	Yes
Flash Tube	HD9450143
Glass cover	clear

Table 6: Specification power supply

Hensel power supply - TRIA 6000S	
Energy	6000J
Shortest lighting time	1/800s
Longest lighting time	1/440s
Head socket	3x Long Plug

5.3 Software

All of the programs and algorithms were written with the programming language Python 3.5. Furthermore, the Python distribution Anaconda 5.0.1 was used to facilitate the analysis of large data sets and the writing of algorithms. The thermograms were recorded with the help of the software *ATIIS* of *Ottronic GmbH*.

5.4 Test specimen

To test the stability and correctness of the developed algorithms, different test plates with partially artificially introduced inhomogeneities were constructed.

5.4.1 Test specimen for testing the stability of the thermal diffusivity α

To test the stability and correctness of the algorithm for the thermal diffusivity, PE-HD-plates with thickness 2mm, 3mm, 5mm, 8mm and 10mm were constructed.

5.4.2 Test specimen for depth estimation

PP-GF - Test plate

The outer dimensions of the test plate were $270 \times 190 \text{mm}^2$ and its thickness was 2 and 4 mm. Polypropylene (*PP*) was used as matrix material and glass fibre (*GF*) was used as fibre material. When measuring the test plate thickness, it was found that this varies by up to $\pm 0.2 \text{mm}$. The positions of the artificially introduced inhomogeneities are shown in figure 33. Different materials or drills of the inhomogeneities are supposed to simulate different defect types, which are shown in table 7.

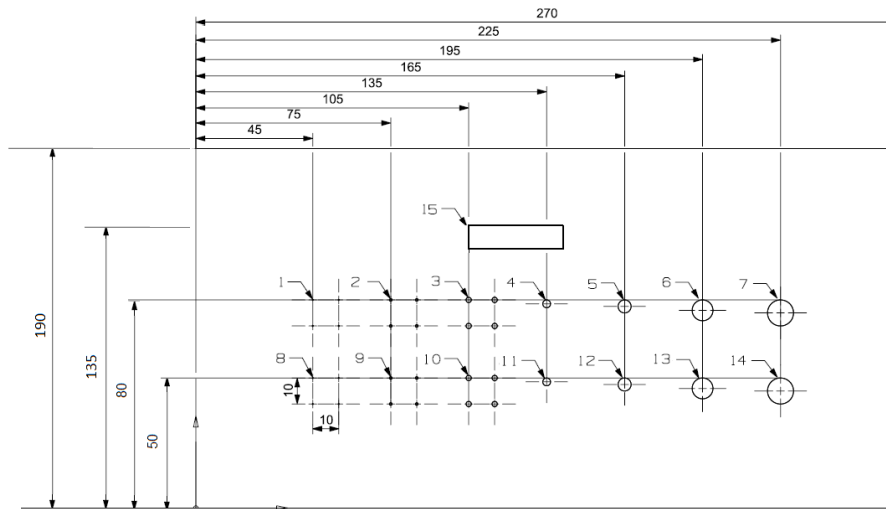


Figure 33: Positions of artificially introduced inhomogeneities

Table 7: Positions and kinds of inhomogeneities

#	Length in mm	Width in mm	Thickness in mm	Depth in mm	Material	Defect-Type
1	4 x 0,5			1	Drill	Cluster of pores
2	4 x 1			1	Drill	Cluster of pores
3	4 x 2			1	Drill	Cluster of pores
4	3			1	Drill	Defect
5	5			1	Drill	Defect
6	8			1	Drill	Defect
7	10			1	Drill	Defect
8	4 x 0,5			0,5	Drill	Cluster of pores
9	4 x 1			0,5	Drill	Cluster of pores
10	4 x 2			0,5	Drill	Cluster of pores
11	3			0,5	Drill	Defect
12	5			0,5	Drill	Defect
13	8			0,5	Drill	Defect
14	10			0,5	Drill	Defect
15	40 x 10 x 0,3			1	GF-Tape	Extraneous material

PA6-GF - Test plate

The outer dimensions of the test plate again were $270 \times 190 \text{ mm}^2$ and its thickness 2 and 4 mm. Polyamide 6 (PA6) was used as matrix material and glass

fibre (*GF*) was used as fibre material. The positions of the artificially introduced inhomogeneities are the same as at PPGF-plate (see figure 33) and again the different types and kinds of the inhomogeneities are shown in table 7.

PE-HD - perforated plate

This PEHD (Polyethylene Hard Density) plate was used to test the stability of the algorithms developed for depth determination. The dimension and the arrangement of the drills can be seen in figure 34. The gradations of the depth of the drills can be seen in figure 35.

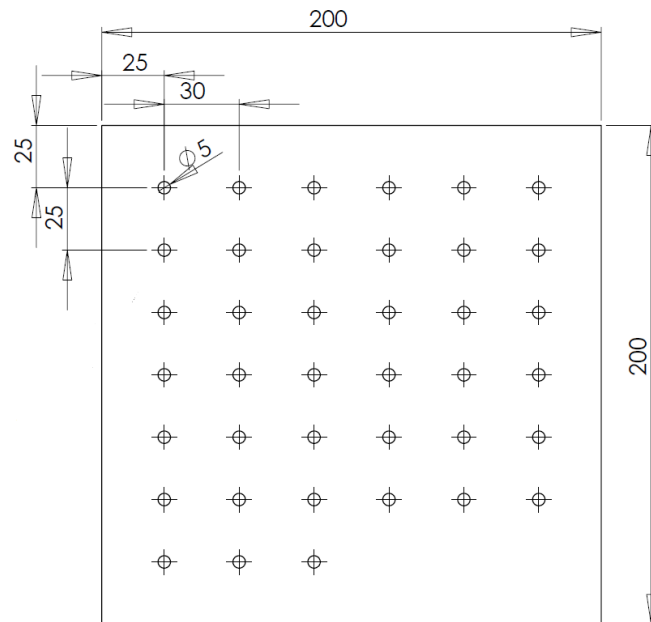


Figure 34: Dimension and arrangement of drills - PEHD

0,46	0,42	0,51	0,68	0,88	1,03
⊕	⊕	⊕	⊕	⊕	⊕
1,33	1,48	1,70	1,90	2,09	2,23
⊕	⊕	⊕	⊕	⊕	⊕
2,53	2,74	2,87	3,08	3,12	3,49
⊕	⊕	⊕	⊕	⊕	⊕
3,92	4,10	4,29	4,50	4,58	4,79
⊕	⊕	⊕	⊕	⊕	⊕
5,10	5,27	5,46	5,75	5,84	5,98
⊕	⊕	⊕	⊕	⊕	⊕
6,35	6,50	6,73	6,89	7,08	7,28
⊕	⊕	⊕	⊕	⊕	⊕
7,50	7,76	7,98			
⊕	⊕	⊕			

Figure 35: Gradiation of depths - PEHD

6 Experiments and Results

6.1 Experiments and results of the implemented Contrast Methods

Algorithms for extracting inhomogeneities and defects may be sensitive to inhomogeneous excitation and the contrast between error and defect-free background vanishes. In order to be able to use these algorithms in their full strength, contrast methods were implemented which attempt to compensate the inhomogeneous excitation.

All algorithms were applied to the test objects described in chapter 5 and tested for their usability. Since algorithms that are sensitive to inhomogeneous excitation, contain a similar spatial pattern in the error-free background, these were checked for spatial homogeneity.

In this section, the results are shown for a PA6-GF specimen. Furthermore a horizontal plot of the pixel $y = 348$ is shown to get a better feeling for the temporal stability of the method. The thermogram sequence was recorded with an acquisition frequency of $100Hz$ and a time of 15 seconds. In the figures of all contrast methods, two different time stamps were chosen (5 seconds after excitation and 10 seconds after excitation) to show the temporal stability.

In figure 36 and figure 37, the non - manipulated thermograms at time stamp 5 second and 10 second after excitation can be seen. Furthermore, all of the images are displayed with pseudo color and the colormap *jet*.

Absolute Contrast

The first result of the Absolute Contrast method can be seen in figure 38 and figure 39. The calculation rule can be seen in 4.6.1.

Running Contrast

The scaled version of the previous contrast method is Running Contrast (4.6.2). The result of this version is shown in figure 40 and figure 41.

Normalized Contrast A

Normalized Contrast A (4.6.3) is the first version of two different normalized methods and the result can be seen in figure 42 and figure 43.

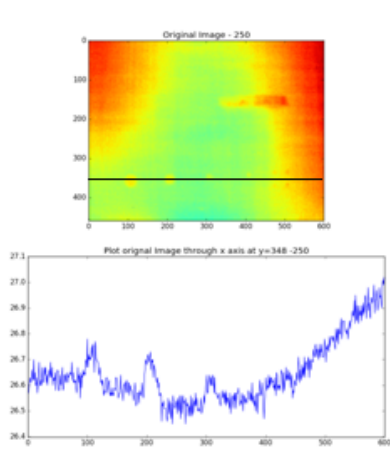


Figure 36: Original thermogram at 5 seconds after excitation

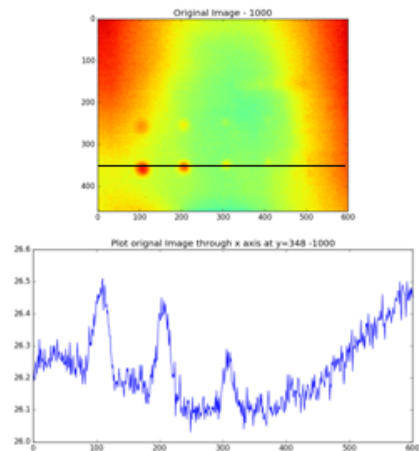


Figure 37: Original thermogram at 10 seconds after excitation

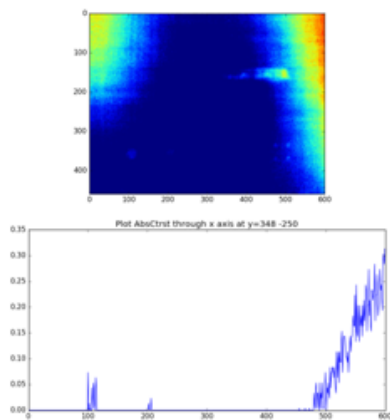


Figure 38: Thermogram manipulated with Absolute Contrast at 5 seconds after excitation

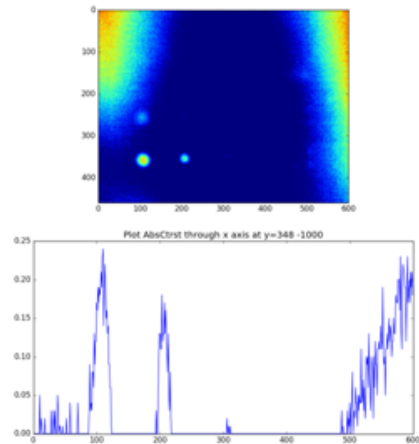


Figure 39: Thermogram manipulated with Absolute Contrast at 10 seconds after excitation

Normalized Contrast B

Normalized Contrast B (4.6.3) is the second version of normalized contrast methods and the results are shown in figure 44 and figure 45.

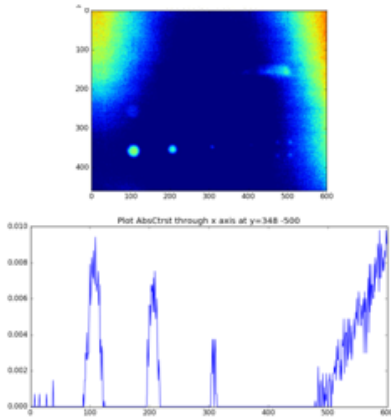


Figure 40: Thermogram manipulated with Running Contrast at 5 seconds after excitation

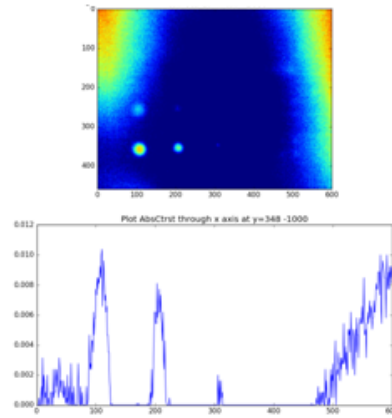


Figure 41: Thermogram manipulated with Running Contrast at 10 seconds after excitation

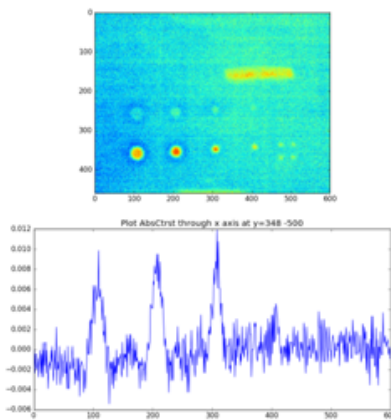


Figure 42: Thermogram manipulated with Normalized Contrast A at 5 seconds after excitation

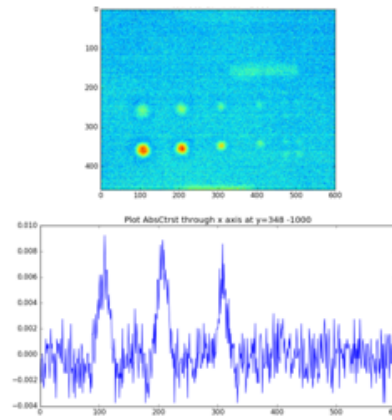


Figure 43: Thermogram manipulated with Normalized Contrast A at 10 seconds after excitation

Standard Contrast

The last contrast method which depends on the selection of a background is Standard Contrast. The result can be seen in figure 46 and figure 47.

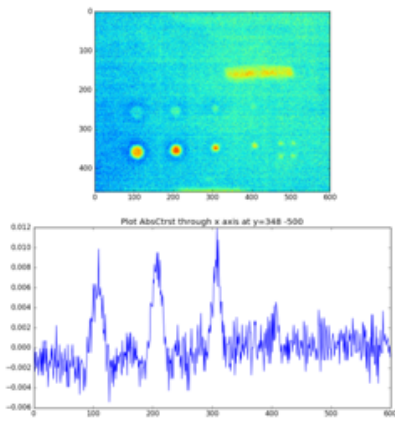


Figure 44: Thermogram manipulated with Normalized Contrast B at 5 seconds after excitation

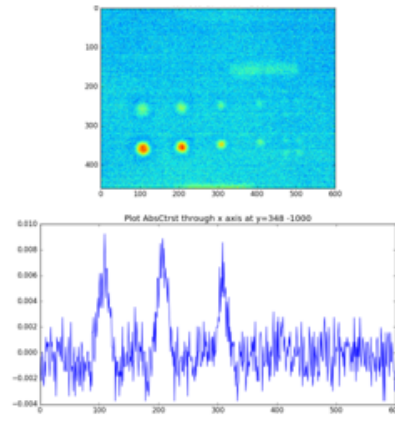


Figure 45: Thermogram manipulated with Normalized Contrast B at 10 seconds after excitation

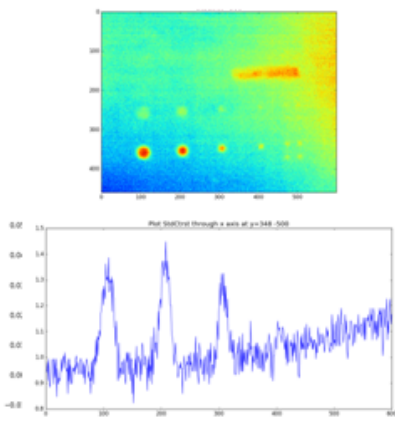


Figure 46: Thermogram manipulated with Standard Contrast at 5 seconds after excitation

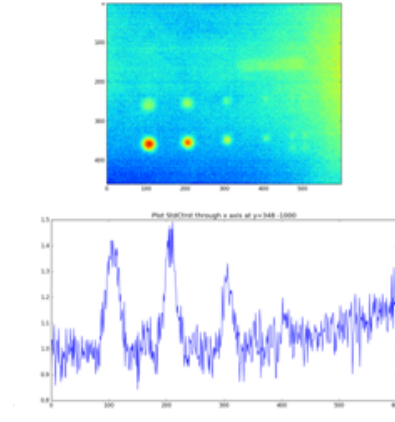


Figure 47: Thermogram manipulated with Standard Contrast at 10 seconds after excitation

Differentiated Absolute Contrast (DAC)

Differentiated Absolute Contrast is the last implemented contrast method in this thesis. It is the only method that does not require any knowledge of

flawless background of the specimen. The results are shown in figure 48 and figure 49.

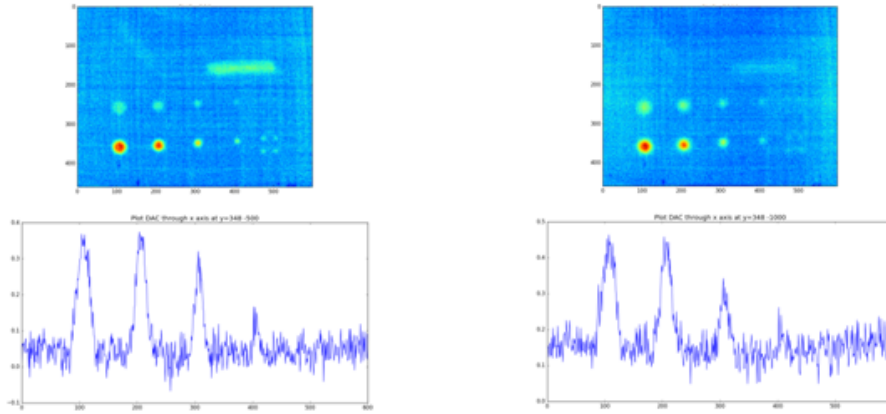


Figure 48: Thermogram manipulated with DAC at 5 seconds after excitation

Figure 49: Thermogram manipulated with DAC at 10 seconds after excitation

6.2 Determination of the thermal diffusivity α

If one reads chapter 4 one recognizes that the material parameter, thermal diffusivity α , plays an important role in the heat theory. It is the key parameter to correctly simulate the heat equation or to determine the depth of inhomogeneities. The algorithm to determine the thermal diffusivity α is described in section 4.7.

To specify the stability and correctness of the algorithm, it was tested at the PE-HD plates which are described in section 3.4.1. The test object was intentionally illuminated as inhomogeneously as possible. Various areas are intended to provide information about the independence of the excitement intensity (see figure 50).

In table 8 to 12 the result of the determined thermal diffusivities for different areas and different thickness of PE-HD plates are outlined. In addition, the tables show the mean and standard deviation of the nine areas of each PE-HD specimen. Table 13 shows the mean value and the standard deviation of the total amount of the PE-HD plates.

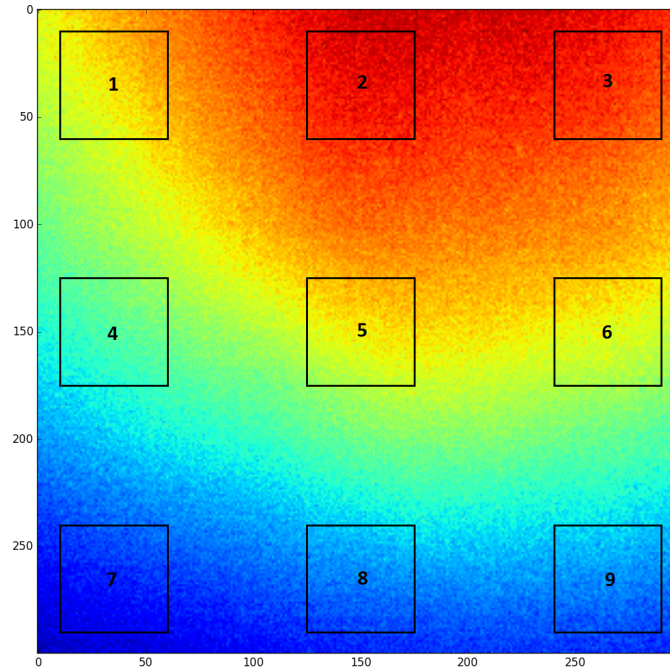


Figure 50: Inhomogeneous illumination and areas to test stability and correctness of α

Table 8: Thermal diffusivity α of specimen PE-HD -2mm

PE-HD - 2mm	
Area	Thermal diffusivity α in $\frac{mm^2}{s}$
1	0.27257
2	0.27527
3	0.27913
4	0.27215
5	0.27455
6	0.27916
7	0.27042
8	0.27342
9	0.27748
Mean:	0.27491
Standard deviation:	0.00294

Table 9: Thermal diffusivity α of specimen PE-HD -3mm

PE-HD - 3mm	
Area	Thermal diffusivity α in $\frac{mm^2}{s}$
1	0.25577
2	0.25738
3	0.25952
4	0.25872
5	0.25903
6	0.26152
7	0.26116
8	0.26148
9	0.26364
Mean:	0.25980
Standard deviation:	0.00226

Table 10: Thermal diffusivity α of specimen PE-HD -5mm

PE-HD - 5mm	
Area	Thermal diffusivity α in $\frac{mm^2}{s}$
1	0.28548
2	0.28761
3	0.28961
4	0.28429
5	0.28502
6	0.28766
7	0.28747
8	0.28716
9	0.28896
Mean:	0.28703
Standard deviation:	0.0016

Table 11: Thermal diffusivity α of specimen PE-HD -8mm

PE-HD - 8mm	
Area	Thermal diffusivity α in $\frac{mm^2}{s}$
1	0.25462
2	0.25476
3	0.25316
4	0.25386
5	0.25609
6	0.25690
7	0.25882
8	0.25886
9	0.25954
Mean:	0.25629
Standard deviation:	0.00223

Table 12: Thermal diffusivity α of specimen PE-HD -10mm

PE-HD - 10mm	
Area	Thermal diffusivity α in $\frac{mm^2}{s}$
1	0.27741
2	0.27797
3	0.27925
4	0.27723
5	0.27664
6	0.27892
7	0.27851
8	0.27952
9	0.28061
Mean:	0.27845
Standard deviation:	0.00118

Table 13: Overall mean and standard deviation of PE-HD

PE-HD - Overall	
Mean:	0.271300663
Standard deviation:	0.012932078

As can be seen in Tables 8 to 12, the standard deviations of the thermal diffusivity of all samples have a very small value. Thus, it can be concluded that all nine tested surfaces are close to the mean, despite different excitation energy and independent of the energy that acts on the test object.

The mean thermal diffusivity of all thicknesses is $0.271 \frac{mm^2}{s}$ and the standard deviation is 0.0129 as illustrated in Table 13. It is striking that the standard deviation of the mean values of different thicknesses is greater than the standard deviation of the heat diffusivities of different excitation energies.

As shown in Chapter 4.3, the thermal diffusivity calculation consists of two unknown, the time $t_{1/2}$ and the thickness L , where the time $t_{1/2}$ is obtained from the experiment. So only the thickness L remains, which is measured manually and is included quadratically in the calculation. Thus, measurement inaccuracies of manual thickness measurement are included quadratically in the calculation and cause a larger standard deviation.

In order to obtain an even more accurate statement about the stability, additional plates PA6-GF - 2mm and PA6-GF - 4mm with different flash distances were measured. Again, different areas were chosen to investigate a possible change in diffusivity depending on the flash energy. A thermogram of the areas can be seen in figure 51. Table 14 and table 15 show the result for the flash distance 15cm and 25cm. Furthermore, table 16 shows the mean value and standard deviation for these two distances. The same results for PA6-GF - 4mm can be seen in table 17, table 18 and table 19.

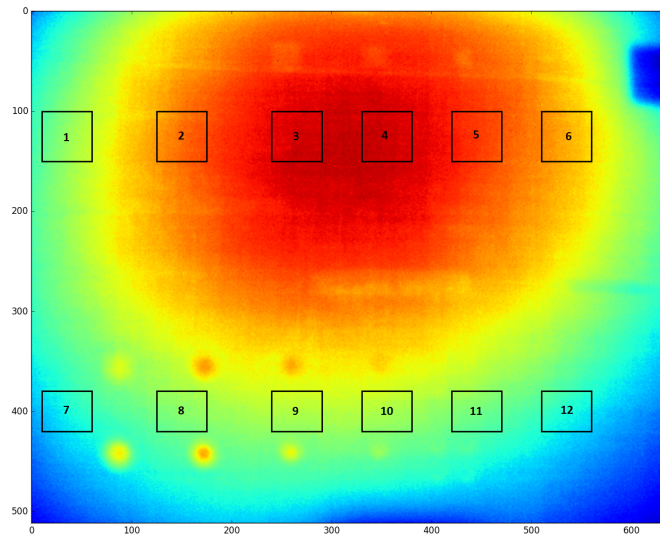


Figure 51: Inhomogeneous illumination and areas of PA6-GF specimen α

Table 14: Thermal diffusivity α of specimen PA6-GF 2mm -15cm flash distance

PA6GF 2mm - 15cm	
Area	Thermal diffusivity α in $\frac{mm^2}{s}$
1	0.28298
2	0.26089
3	0.24195
4	0.24067
5	0.24881
6	0.26698
7	0.31502
8	0.29416
9	0.27595
10	0.27355
11	0.28164
12	0.29675
Mean:	0.27328
Standard deviation:	0.02186

Table 15: Thermal diffusivity α of specimen PA6-GF 2mm -25cm flash distance

PA6-GF 2mm - 25cm	
Area	Thermal diffusivity α in $\frac{mm^2}{s}$
1	0.30680
2	0.28072
3	0.25767
4	0.25766
5	0.26353
6	0.28124
7	0.33292
8	0.30880
9	0.28827
10	0.28337
11	0.28940
12	0.30189
Mean:	0.28769
Standard deviation:	0.02152

Table 16: Overall mean and standard deviation of PA6-GF - 2mm

PA6-GF 2mm - Overall	
Mean:	0.28048
Standard deviation:	0.01018

Table 17: Thermal diffusivity α of specimen PA6-GF 4mm -15cm flash distance

PA6-GF 4mm - 15cm	
Area	Thermal diffusivity α in $\frac{mm^2}{s}$
1	0.31210
2	0.28345
3	0.26799
4	0.26123
5	0.26481
6	0.26290
7	0.29654
8	0.27189
9	0.26401
10	0.26706
11	0.26961
12	0.27230
Mean:	0.27449
Standard deviation:	0.01479

Table 18: Thermal diffusivity α of specimen PA6-GF 4mm -25cm flash distance

PA6-GF 4mm - 25cm	
Area	Thermal diffusivity α in $\frac{mm^2}{s}$
1	0.31609
2	0.29420
3	0.27509
4	0.26664
5	0.26354
6	0.27008
7	0.29818
8	0.27131
9	0.26472
10	0.26001
11	0.26131
12	0.26906
Mean:	0.27585
Standard deviation:	0.01677

Table 19: Overall mean and standard deviation of PA6-GF - 4mm

PA6-GF 4mm - Overall	
Mean:	0,27517
Standard deviation:	0,00096

In this experiment, the effect of different flash to object distances on the thermal diffusivity of the PA6-GF plates 2mm and 4mm can be observed. As can be seen in Table 16 for 2mm and Table 19 for 4mm, different distances on each of the twelve areas tested do not greatly affect the thermal diffusivity. It is noticeable, however, that individual areas deviate more than in the experiments with the PE-HD objects.

This is because measuring the PA6-GF plate has revealed a greater variance in thickness across the entire plate. Due to the fact that the thickness is taken quadratically in the calculation, a constant assumed thickness causes errors which cause a quadratic error of thermal diffusivity.

6.3 Implementation of Heat equation with finite differences

In chapter 4.8, various methods were presented which show how to implement the heat equation with finite differences. In this work, the simulation is used to increase the contrast between background and inhomogeneities and as part of the depth determination of inhomogeneities. Figure 52 shows the thermogram 5 seconds after excitation and figure 53 shows the temporal profile of the flawless background and the three inhomogeneities. First, the 1D-implicit heat equation of each pixel was simulated and subtracted with the original signal of cooling process. Each simulation of the heat equation was based on the previously determined α -value

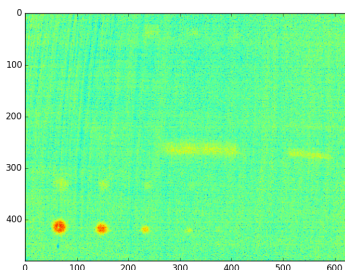


Figure 52: Thermogram 5 seconds after excitation with subtracted heat simulation

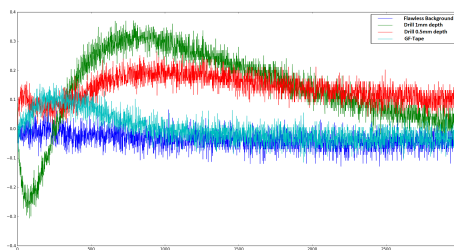


Figure 53: Temporal profile of flawless background, drill in 1mm depth, drill in 0.5mm depth and GF-Tape

6.3.1 1D-Heat equation with explicit method

To simulate this method, we assume a long thin rod whose length is scaled to the range $[0, 1]$. The thermal diffusivity α is given by the value $\alpha = 1e - 5$. The initial condition can be seen in figure 54 and the boundary conditions are *Dirichlet*-boundary conditions with $b_0 = s$ and $b_1 = s$ where s is the scaling factor, given as $\frac{\alpha \Delta t}{\Delta x^2}$. In figure 57, the temporal heat flow of the rod can be seen. After about 12000 seconds, the stability condition is reached.

6.3.2 1D-Heat equation with implicit method

In this method, again we assume a thin rod whose length is again scaled to the range $[0, 1]$. Furthermore, we assume the same thermal diffusivity $\alpha = 1e - 5$ and the same initial condition, as can be seen in figure 56. Compared to

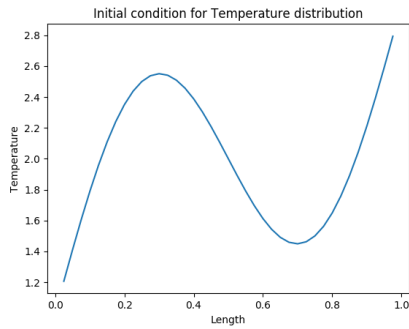


Figure 54: 1D Explicit method - Initial condition

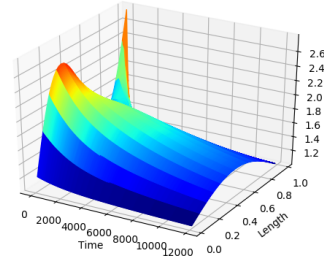


Figure 55: 1D Explicit method - Stability condition

the simulation of the explicit method, the difference is that we assume this time *Neumann*-boundary conditions. With this boundary conditions, the tridiagonal matrix is modified by $A[0, 1] = -2s$ and $A[n, n - 1] = -2s$. The term n is thereby the number of grid points. In this simulation, the boundary condition vector b is assumed to be $b_0 = 3 \cdot 2 \cdot s\Delta x$ and $b_1 = 3 \cdot 2 \cdot s\Delta x$. The scaling factor s is given as $\frac{\alpha\Delta t}{\Delta x^2}$. The heat distribution after 12 000 seconds of the heat flow can be seen in figure 57.

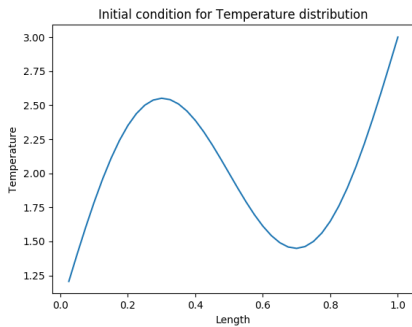


Figure 56: 1D Implicit method - Initial condition

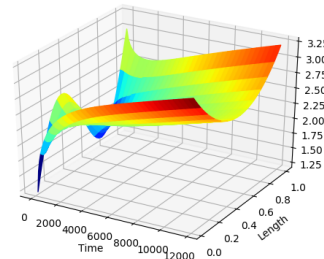


Figure 57: 1D Implicit method - Stability condition

6.3.3 2D-Heat equation with explicit method

In the following test, instead of a rod, a thin plate is taken. The lengths x and y are scaled between the range $[0, 1]$. To show the two-dimensional heat

equation with the explicit method we assume a constant initial condition of $0C$ of the thin plate, as can be seen in figure 58 . As described in section 4.8, the explicit methods are subject to a condition of stability. For the one-dimensional heat equation, is it $\Delta t \leq \frac{(\Delta x)^2}{2 \cdot \alpha}$ and for the two-dimensional case it is $\Delta t \leq \frac{h^2}{4 \cdot \alpha}$. If the right term is smaller than the left one, the stability condition is violated. Now we simulate the two-dimensional explicit heat equation where two points of the plate are heated and one point of the plate is cooled and the stability condition is violated. The result can be seen in figure 59.

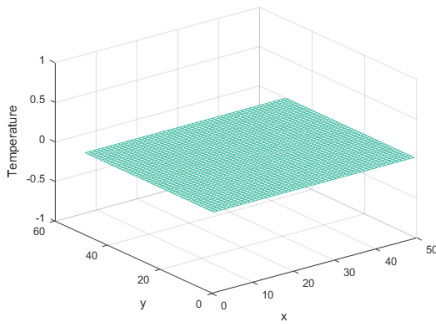


Figure 58: 2D Explicit method - Initial condition

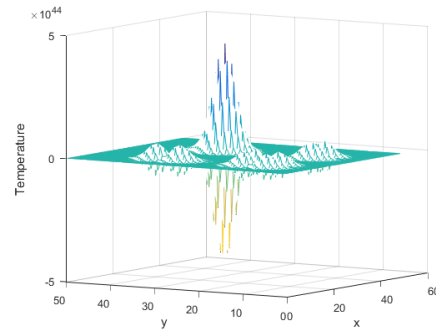


Figure 59: 2D Explicit method - Stability condition with violated stability condition

6.3.4 2D-Heat equation with implicit method

The advantage of this method is that the implicit methods are not subject to any stability condition. The same experiment is simulated similar to chapter 5.3.3. A thin plate, with initial temperature $0C$ (see figure 60), is heated at two areas and cooled at one area. The boundaries of the plate are kept at a constant value of $0C$. As can be seen from figure 61, there is no violation of a stability condition.

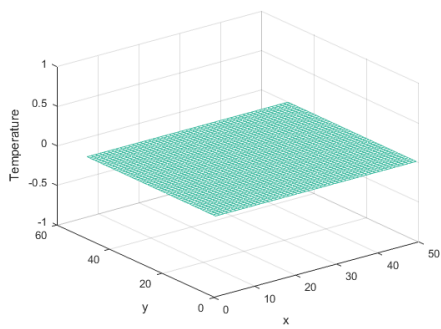


Figure 60: 2D Implicit method - Initial condition

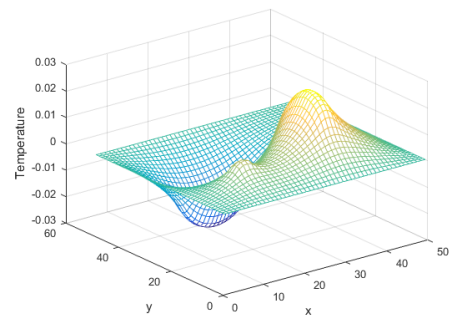


Figure 61: 2D Implicit method - Stability condition

6.4 Depth determination

6.4.1 Preliminary observation

In order to derive a statement about the quality of the different depth determination methods, holes were drilled in different depths in an 8mm PE-HD plate. All depths in all specimen were measured by hand and used as reference point. In figures 62 to figure 73, the temporal profile of a flawless background and the temporal profiles of the inhomogeneities can be seen. As can be seen in the temporal profiles, the difference between error-free background and inhomogeneity decreases with increasing depth until no difference is recognizable. For this reason, the results of the depth calculation of different methods only deal with different depths as long as differences are recognizable.

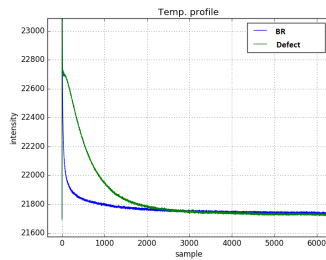


Figure 62: Temporal profile of flawless background and inhomogeneity in 0.02mm depth

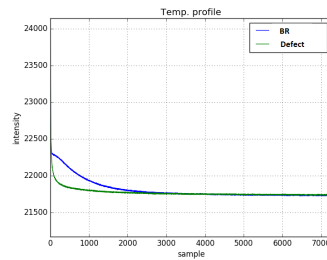


Figure 63: Temporal profile of flawless background and inhomogeneity in 0.24mm depth

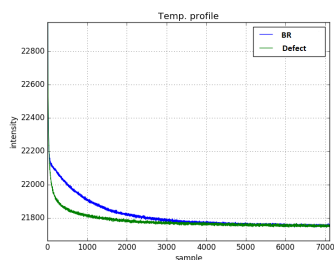


Figure 64: Temporal profile of flawless background and inhomogeneity in 0.5mm depth

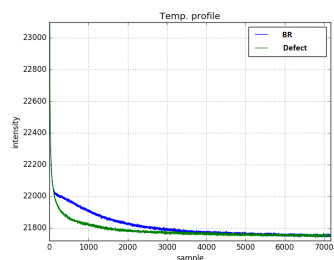


Figure 65: Temporal profile of flawless background and inhomogeneity in 0.72mm depth

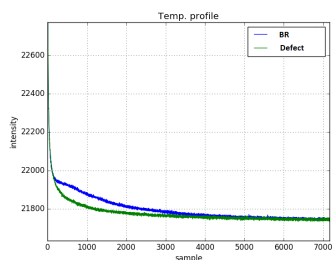


Figure 66: Temporal profile of flawless background and inhomogeneity in 0.92mm depth

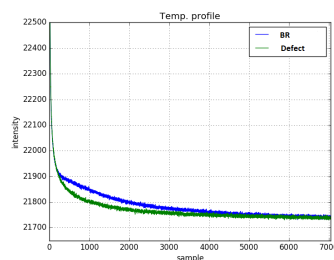


Figure 67: Temporal profile of flawless background and inhomogeneity in 1.11mm depth

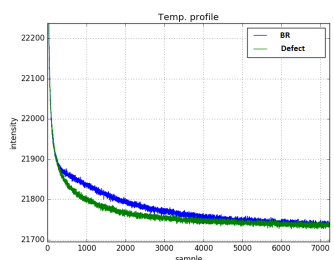


Figure 68: Temporal profile of flawless background and inhomogeneity in 1.27mm depth

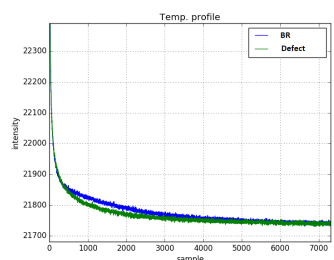


Figure 69: Temporal profile of flawless background and inhomogeneity in 1.5mm depth

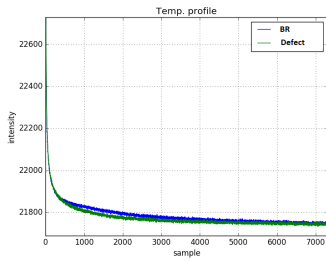


Figure 70: Temporal profile of flawless background and inhomogeneity in 1.75mm depth

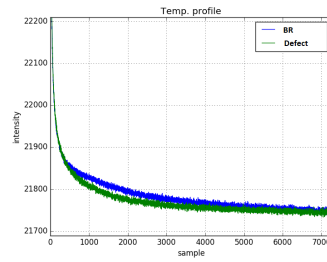


Figure 71: Temporal profile of flawless background and inhomogeneity in 2.02mm depth

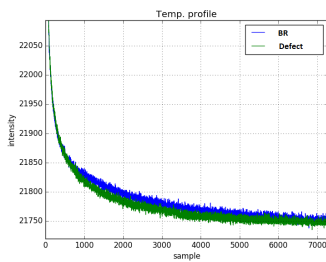


Figure 72: Temporal profile of flawless background and inhomogeneity in 2.16mm depth

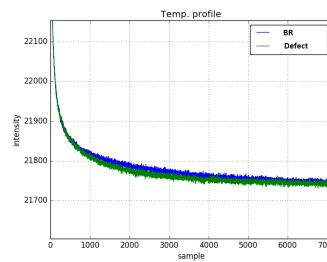


Figure 73: Temporal profile of flawless background and inhomogeneity in 2.25mm depth

6.4.2 LSD - depth determination

To check this algorithm for correctness, equation 103 was used to simulate inhomogeneities. Inhomogeneities in the depth of $1mm$, $2mm$ and $3mm$ were simulated as well as signals without noise and signals with a signal to noise ratio (SNR) of $40dB$, $30dB$ and $20dB$. In order to test the robustness of this method by the degree of the polynomial of the TSR, each simulated signal was additionally fitted with the polynomial 5 to 20.

In figure 74, the noise free simulated signal with an inhomogeneity of $2mm$ and the fitted signal with TSR and polynom 10 can be seen. Furthermore, figure 75 shows the determined depth of the LSD method with numerical and analytical derivation.

Again the depth determination with the LSD method can be seen in figure 76 and figure 77 with a SNR of $20dB$. Problems with this method result from a combination of a high proportion of noise ($\leq 20dB$) and a high degree of the polynomial of the TSR. This problem can be seen in figure 78 and figure 79, where an inhomogeneity of $3mm$ was simulated and the simulated signal is manipulated with noise ($SNR = 20dB$). In figure 79 the wrong determined signal can be seen.

Due to the large number of pictures, the remaining results can be found on the web.

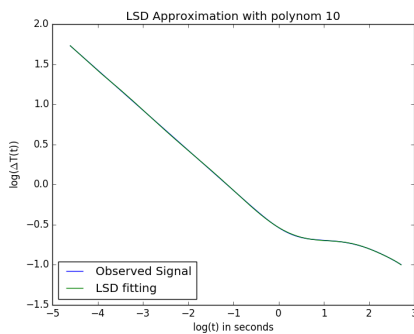


Figure 74: Noise free simulated signal and TSR with an inhomogeneity of $2mm$

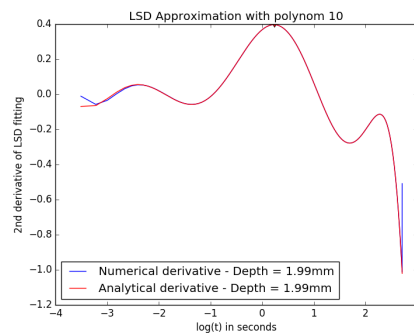


Figure 75: Determined depth with LSD of inhomogeneity with numerical and analytical derivation

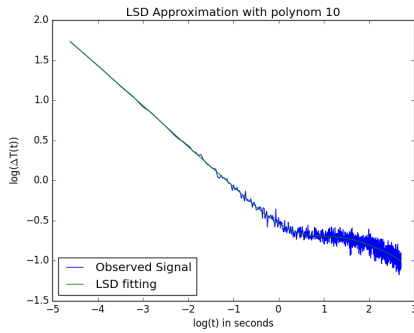


Figure 76: Simulated signal with a SNR of $20dB$ and TSR with an inhomogeneity of 2mm

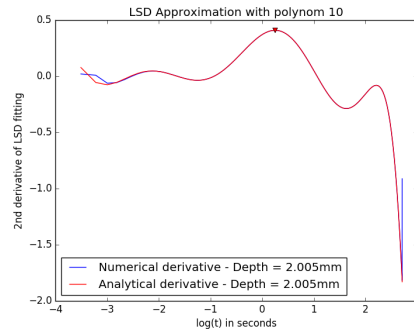


Figure 77: Determined depth with LSD of inhomogeneity with numerical and analytical derivation

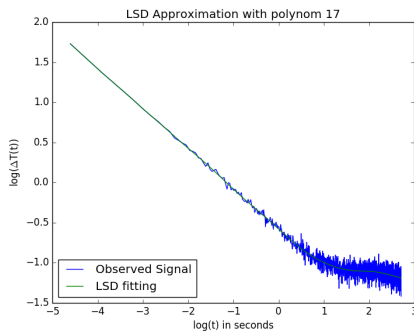


Figure 78: Simulated signal with a SNR of $20dB$ and TSR with an inhomogeneity of 3mm

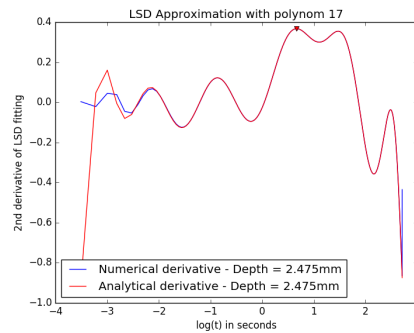


Figure 79: Determined depth with LSD of inhomogeneity with numerical and analytical derivation

After the check of the algorithm with simulations, the algorithm was tested at the test plates which are described in section 3.4. In figure 80, a schematic representation of the depth determination can be seen. The determined depths of the PP-GF - 2mm specimen with LSD is shown in table 20.

In figure 81, the temporal curve of a flawless background pixel and a drill in 2mm depth of a PP-GF plate with 4mm thickness is depicted. Because of the small differences in the cooling curves, no exact depth can be determined at this test object.

The result of the depth determination of the PA6-GF - 2mm plate is shown

in table 21. Due to the too small differences between flawless background and inhomogeneity, this test object could not get a result for the depth of the matrix accumulation. The same effect can be seen in figure 81.

Furthermore the result of the depth determination of the PA6-GF - 4mm plate is shown in table 22. Again no depth of the matrix accumulation can be determined.

The last specimen that was tested with this method was the PE-HD plate with drills. The results of depth determination are shown in table 23.

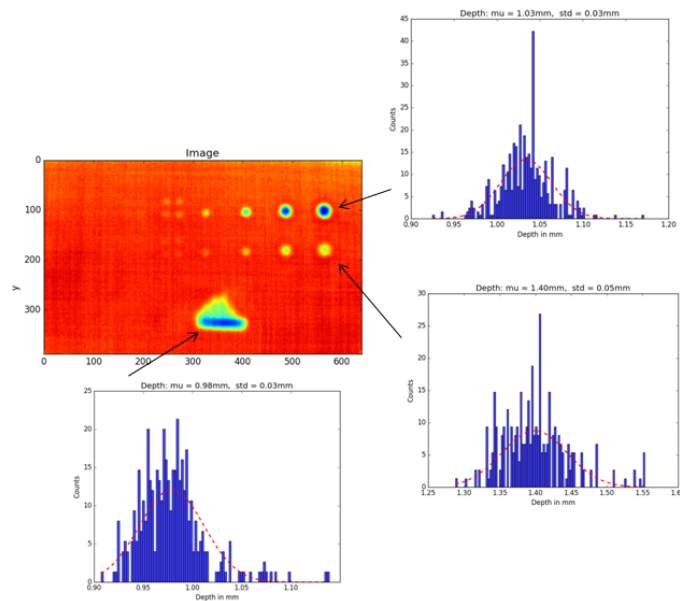


Figure 80: Schematic representation of depth estimation with LSD - PP-GF 2mm

Table 20: Depth calculation with LSD - PP-GF 2mm

	Measured depth in mm	Calculated Mean in mm	Standard Deviation in mm
Drill 1	1.11	1.03	0.03
Drill 2	1.55	1.40	0.05
Matrix Accumulation	1	0.98	0.03

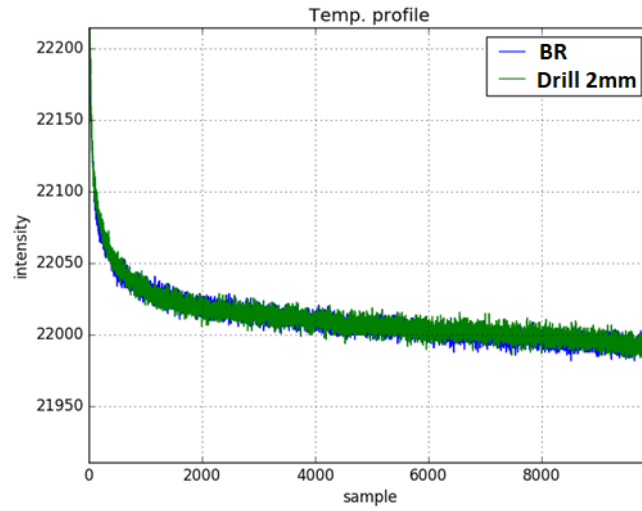


Figure 81: Cooling curves of flawless background and drill in 2mm depth - PP-GF 4mm

Table 21: Depth calculation with LSD - PA6-GF 2mm

	Measured depth in mm	Calculated Mean in mm	Standard Deviation in mm
Drill 1	1.35	1.20	0.12
Drill 2	1.88	1.81	0.27

Table 22: Depth calculation with LSD - PA6-GF 4mm

	Measured depth in mm	Calculated Mean in mm	Standard Deviation in mm
Drill 1	1.94	2.07	0.11
Drill 2	2.83	3.13	0.15

Table 23: Depth determination of PE-HD plate with LSD

Measured depth in mm	Determined Mean in mm	Standard Deviation in mm
0.02	0.11	0.07
0.24	0.25	0.09
0.5	0.55	0.11
0.72	0.82	0.09
0.92	0.94	0.12
1.11	1.2	0.12
1.27	1.32	0.21
1.5	1.47	0.26
1.75	1.71	0.28
2.02	1.82	0.33
2.16	1.96	0.37
2.25	1.98	0.72
2.54	2.02	0.96
2.73	1.98	0.89
2.90	1.95	1.05
3.21	2.17	0.98

6.4.3 APST - depth determination

The second method for depth determination was again tested first with simulated signals and with the same parameters as described in section 5.4.1.

In figure 82, the noise free simulated signal with an inhomogeneity of 2mm and the fitted signal with polynomial fit and polynom 10 can be seen. Furthermore, figure 83 shows the determined depth of the APST method with numerical and analytical derivation.

Again the depth determination with the LSD method can be seen in figure 84 and figure 85 with a SNR of 20dB.

Applying this method, problems arise because of a combination of a high proportion of noise ($\leq 20dB$) and a high degree of the polynomial of the polynomial fit. This problem can be seen in figure 86 and figure 87, where an inhomogeneity of 3mm is simulated and the simulated signal is manipulated with noise (SNR = 20dB). In figure 87, the wrong determined signal can be seen.

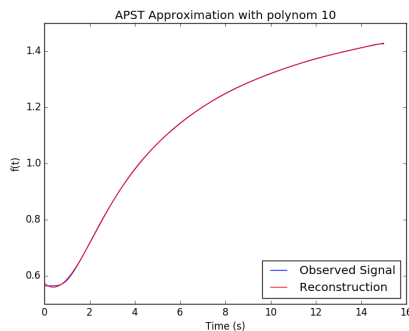


Figure 82: Noise free simulated signal and polynomial fit with an inhomogeneity of 2mm

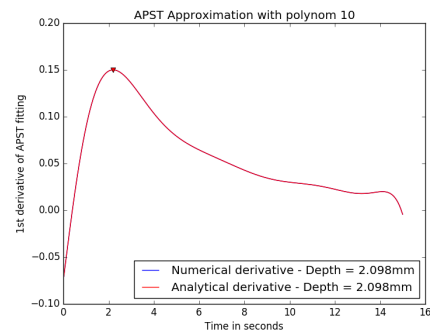


Figure 83: Determined depth with APST of inhomogeneity with numerical and analytical derivation

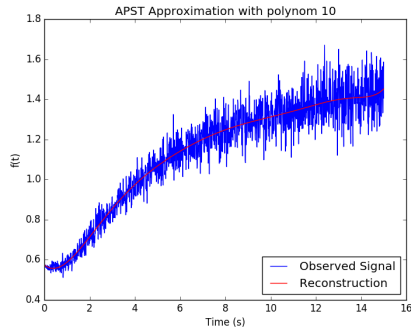


Figure 84: Simulated signal with a SNR of $20dB$ and polynomial fit with an inhomogeneity of $2mm$

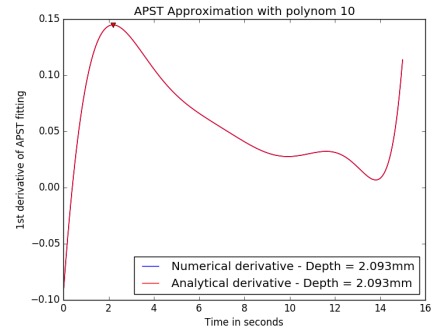


Figure 85: Determined depth with APST of inhomogeneity with numerical and analytical derivation

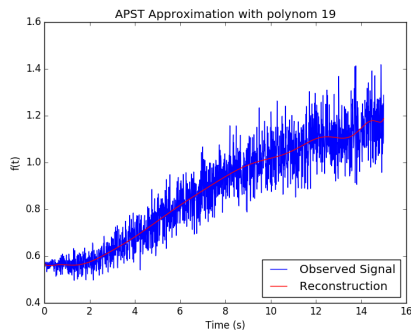


Figure 86: Simulated signal with a SNR of $20dB$ and a polynomial degree of 19 with an inhomogeneity of $3mm$

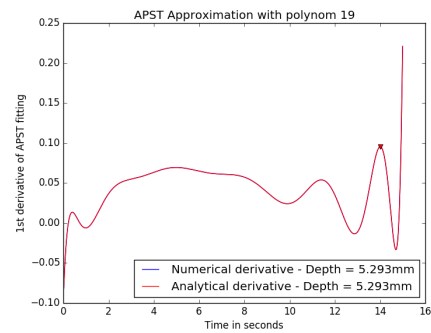


Figure 87: Determined depth with APST of inhomogeneity with numerical and analytical derivation

A schematic representation of the depth determination by means of APST and the test specimen as described in section 3.4 is shown in figure 88. The results of the depth determination of the PP-GF specimen with a thickness of 2mm are shown in table 24.

As described in section 5.4.1 and as depicted in figure 81, it is not possible to determine the depths of the inhomogeneities of the PP-GF specimen with 4mm thickness.

The next specimen is the PA6-GF plate with a thickness of 2mm and 4mm. The results are shown in table 25 and table 26.

Again, this algorithm was tested with the created PE-HD specimen and the results of the depth determination, as far as a depth of 2.02mm, are shown in table 27.

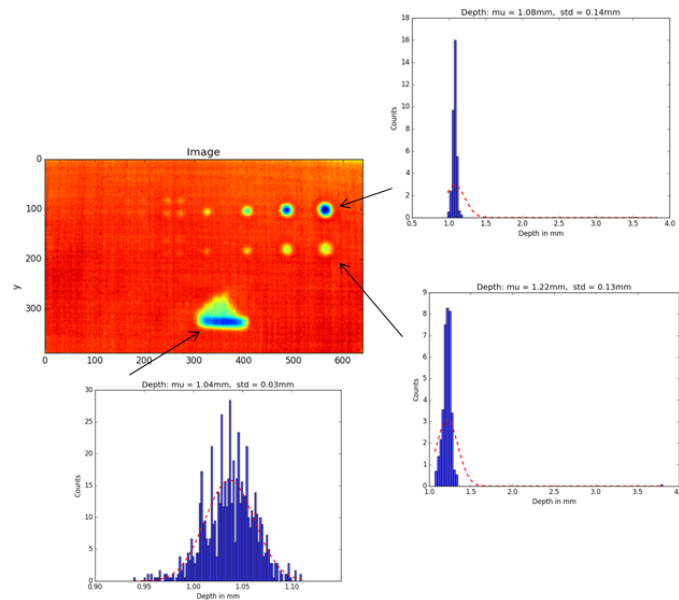


Figure 88: Schematic representation of depth estimation with APST - PP-GF 2mm

Table 24: Depth calculation with APST - PP-GF 2mm

	Measured depth in mm	Calculated Mean in mm	Standard Deviation in mm
Drill 1	1.11	1.08	0.14
Drill 2	1.55	1.22	0.13
Matrix Accumulation	1	1.04	0.03

Table 25: Depth calculation with APST - PA6-GF 2mm

	Measured depth in mm	Calculated Mean in mm	Standard Deviation in mm
Drill 1	1.35	1.23	0.15
Drill 2	1.88	1.75	0.25

Table 26: Depth calculation with APST - PA6-GF 4mm

	Measured depth in mm	Calculated Mean in mm	Standard Deviation in mm
Drill 1	1.94	2.12	1.03
Drill 2	2.83	4.27	0.73

Table 27: Depth determination of PE-HD plate with APST

Measured depth in mm	Determined Mean in mm	Standard Deviation in mm
0.02	0.2	0.02
0.24	0.42	0.03
0.5	0.58	0.01
0.72	0.7	0.02
0.92	0.88	0.11
1.11	1.15	0.02
1.27	1.22	0.02
1.5	1.26	0.02
1.75	0.93	0.31
2.02	0.67	1.09

6.4.4 Maximum Contrast

The last method used in this thesis for depth calculation is the maximum contrast method. This method was not tested with any simulation but with the test specimen as described in section 3.4. Again, a schematic representation of the determined depth can be seen in figure 89.

The depth determination for the specimen PP-GF - 2mm can be seen in table 28. In case of the PP-GF - 4mm plate, again, the same effect as in the two previously described methods occurs, which is that the inhomogeneity signal is almost equal to the flawless background and thus no depth can be determined.

The result for the specimen PA6-GF - 2mm and PA6-GF - 4mm is shown in table 29 and table 30.

Finally also the specimen PE-HD with artificial induced drills were tested and the results can be seen in table 31.

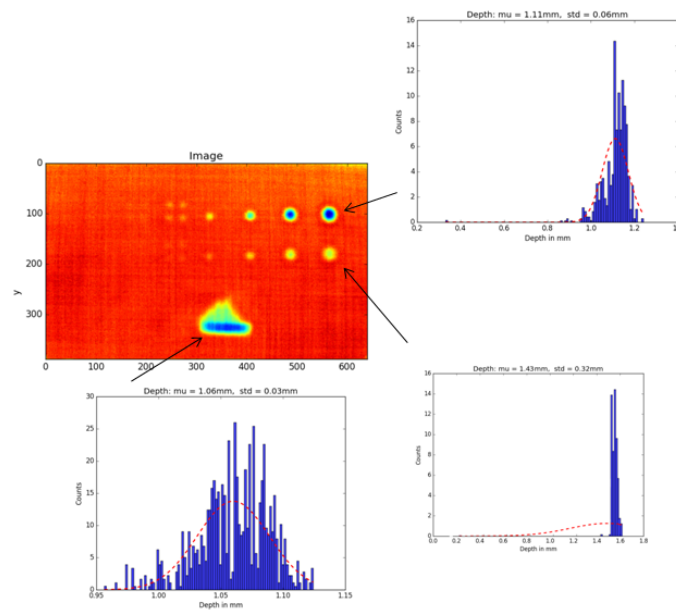


Figure 89: Schematic representation of depth estimation with Maximum Contrast - PP-GF 2mm

Table 28: Depth calculation with Maximum contrast - PP-GF 2mm

	Measured depth in mm	Calculated Mean in mm	Standard Deviation in mm
Drill 1	1.11	1.11	0.06
Drill 2	1.55	1.43	0.14
Matrix Accumulation	1	1.06	0.03

Table 29: Depth calculation with Maximum Contrast - PA6-GF 2mm

	Measured depth in mm	Calculated Mean in mm	Standard Deviation in mm
Drill 1	1.35	1.28	0.07
Drill 2	1.88	1.46	0.32

Table 30: Depth calculation with Maximum Contrast - PA6-GF 4mm

	Measured depth in mm	Calculated Mean in mm	Standard Deviation in mm
Drill 1	1.94	1.78	0.13
Drill 2	2.83	3.57	1.02

Table 31: Depth determination of PE-HD plate with Maximum Contrast

Measured depth in mm	Determined Mean in mm	Standard Deviation in mm
0.02	0.32	0.12
0.24	0.36	0.08
0.5	0.51	0.05
0.72	0.68	0.03
0.92	0.92	0.01
1.11	1.03	0.02
1.27	1.14	0.01
1.5	1.41	0.03
1.75	1.80	0.09
2.02	1.93	0.22
2.16	2.21	0.30
2.25	2.47	0.52
2.54	2.97	0.48
2.73	3.15	0.79

7 Conclusion and Discussion

7.1 Discussion of the results

7.1.1 Contrast methods

As described in chapter 4.6, basically two types of contrast methods are presented and implemented in this thesis to improve the contrast between flawless background and inhomogeneities. On the one hand, there are contrast methods which require the selection of a background without inhomogeneity (Absolute Contrast, Running Contrast, Normalized Contrast A, Normalized Contrast B and Standard Contrast) and on the other hand, in this thesis a contrast method is implemented which requires a temporal reference point until the first defect occurs (DAC) which is derived from the one-dimensional heat equation.

Absolute Contrast and Running Contrast are basically the same methods except that Running Contrast is a scaled version of the Absolute Contrast method. These two methods only work if an ideal homogeneous illumination of the specimen is achieved. If the illumination of the specimen is inhomogeneous and the flawless background is chosen such that the intensity is greater than the intensity of the inhomogeneities, inhomogeneities will be smaller than 0 after subtraction of the background. The condition of these two methods that all pixels smaller than 0 are set to 0, leads to deleting the normally existing inhomogeneities and can therefore no longer be detected. With the Normalized Contrast A method, each pixel is first scaled to the final temperature value, and the selected error-free background is also scaled to the final temperature value. The advantage of this method compared to the absolute contrast and running contrast method is that even negative values are allowed and thus, information is preserved. The function of this method is also dependent on the recording time in addition to the selection of flawless background. If the recording time is infinite, each pixel has the same final temperature and each pixel is scaled to the same value. Thus, this method is then a kind of absolute contrast with scaled values and without the condition.

With the Normalized Contrast B method, each pixel is scaled to the temperature value of the excitation in the pixel. With this procedure, this method is independent from the recording time but still dependent on the choice of flawless background.

The last method that depends on the choice of the flawless background is the method Standard Contrast. In this method, each thermogram and the selected background is subtracted with the temperature of the specimen and

the selected background before the excitation. By doing so, an improvement can be achieved if the test object has already had an inhomogeneous illumination before testing with active thermography. If the test object has had the same temperature everywhere before the test, the result is a scaled version of the original thermograms.

The method Differentiated Absolute Contrast (DAC) is the only method of this thesis that is not dependent on the choice of a flawless background and is derived from the one-dimensional heat equation. In order to simulate the heat equation, the material constant heat diffusivity α is needed. The method DAC assumes that the heat diffusivity is unknown and compensates the unknown term by the time up to which it is assumed that no inhomogeneity is visible. If the depth of inhomogeneities is known, DAC is a stable method to increase the contrast between error-free area and inhomogeneities. If the depths of inhomogeneities are unknown and the time is chosen incorrectly, the thermal diffusivity is estimated wrongly and the method becomes unstable.

7.1.2 Determination of the thermal diffusivity α

In order to correctly simulate the heat equation, a major requirement of this thesis was the correct calculation of thermal diffusivity α . To test the stability and correctness of the calculation, different test methods were defined. First, different thicknesses of the PE-HD plate were tested. In order to make a statement about the behavior of the heat diffusivity in dependence of the inhomogeneous illumination, different areas at the specimen were defined and tested. The result of all plates of the determination can be seen in table 12. Due to the small standard deviation of all measurements, the result was classified as good, reproducible and stable against inhomogeneous illumination. Furthermore, the specimen PA6-GF was tested with different lightning distances and defined areas. Again, there were small standard deviations between the defined areas and the measurements. Thus, the result was classified as good, reproducible and stable against inhomogeneous illumination. In order to obtain an independent result of thermal diffusivity, this test object was further analyzed by laser flash analysis. The result of the laser flash analysis showed a thermal diffusivity of $0.277 \frac{mm^2}{s}$.

In general, the determination of thermal diffusivity using active thermography is a stable method and is already being used in industry. The requirement for accurate determination of thermal diffusivity is an exact thickness of the object to be examined. Due to the quadratic influence of the thickness in the calculation, larger errors in the calculated thermal diffusivity result even from small measuring errors.

7.1.3 Implementation of the heat equation

The heat equation in this thesis is used as an aid to increase the contrast between flawless background and inhomogeneities when inhomogeneous illumination is present at the specimen. On the other hand, it is also used as an aid for the depth determination of inhomogeneities. Due to stability problems of the explicit methods, these methods were mainly avoided in the generation of the results. Jean Baptiste Joseph Fourier described the effect that heat flows from warmer regions to colder regions. If the specimen is now excited with an excitation source, the specimen has a temperature difference at the surface at the time $t = 0$ in relation to the rest of the object. The heat then spreads to the depth. Since the two-dimensional heat equation assumes a thin plate where the heat propagates in space in direction x and y , this results in a contradiction to the Fourier law. Tests have been made with the two-dimensional heat equation but no useful results were achieved. Thus, the law of Fourier was affirmed and the two-dimensional heat equation was excluded for further experiments.

To use the heat equation for active thermography, the selection focused on the one-dimensional implicit and one-dimensional cranck nicolson method. All results of the heat equation were simulated with Neumann boundary conditions with $U(t, 0) = 0 = \frac{\delta U_0^k}{\delta x}$ and $U(t, 1) = 0 = \frac{\delta U_{n+1}^k}{\delta x}$. So for $U(t, 0)$ and $U(t, 1)$, there is an ideal insulator. These boundary conditions are only conditionally valid. Due to the ideal insulator, the heat only spreads into the specimen and is thus still present in the specimen after the time $t = \infty$ and thus cannot return to the basic temperature state. However, when exclusively considering the period of time when interactions between heat flow and inhomogeneities arise, this assumption is a good choice.

The use of finite differences for the approximation of the analytic solution of the heat equation results in a discretization error e , which depends on the step size of the time Δt and the step size of the area-direction Δx as described in chapter 4.4. If small time steps and small area-direction steps are used, the choice of using the Cranck Nicolson through the square in $(\Delta t)^2$ is an advantage and achieves a less discretization error e . However, if time steps greater 1 are selected, the discretization error increases by the factor of the square Δt . Thus, approximations with finite differences achieve better accuracies by means of the implicit method.

7.1.4 Depth determination

In the simulation of the LSD and APST method, the stability of the methods was first examined in dependence on the noise and the degree of the polynomial of the fitting function. The two methods are stable at *No Noise* and a *SNR* of $40dB$ and $30dB$ independent from the polynomial of the fitting function. At a *SNR* of $20dB$, there is a high probability that first problems occur. With this *SNR* and from a polynomial of about 15, the fitted signal adapts to the noise and thus, no exact depth determination can be calculated.

In order to determine the correct depth of inhomogeneities, it is necessary that the signals of inhomogeneities have a significant difference compared to the flawless area. This significant difference depends on the depth of inhomogeneities, the diameter of inhomogeneities, the thermal diffusivity of the specimen and the amount of energy which is induced the specimen. This large number of dependent parameters often makes accurate depth determination difficult. In order to derive a statement about the quality of the different depth determination methods, holes were drilled in different depths in an 8mm PE-HD plate. All depths in all specimen were measured by hand and used as reference point.

With the method LSD, the depth of the PE-HD plate is credibly determined up to a depth of about 2mm. However, the standard deviation increases sharply from a depth of 1.5mm.

The worst results of depth determination of the PE-HD plate are achieved with the method APST. Up to a depth of 1.5mm, the depth of the drills is exactly determined and also the standard deviation is very small.

When determining the depth with the maximum contrast method, the depth to 2.16 mm is determined as accurately as possible. The standard deviation increases from a drill depth of 2.02mm and is previously consistently small. The prerequisite for the functionality of this method, however, is an exact calculation of the thermal diffusivity α .

7.2 Conclusion

Active thermography is a wide-spread but powerful application technique to inspect components non-destructively and quickly. In contrast to the x-ray examination, there are no additional costs and it can therefore be used at any time. The disadvantage is that additional components, such as the excitation source, can strongly influence the results. As shown in this thesis, there are methods to compensate for inhomogeneous illumination. The contrast method DAC is a method that compensates for this inhomogeneous illumination with the help of the heat equation. In all of the contrast methods, however, knowledge about either the placement of inhomogeneities or the depth of inhomogeneities must be present. If this knowledge is not available, problems will arise when applying these methods.

In order to extract features of thermographic sequences and to display them in a single image, the most frequent techniques, such as PPT, PCT, Statistical Parameters and Wavelet-Transform, are briefly presented in this thesis. In order to remove the temporal noise of thermographic images, common fitting methods, such as polynomial fit or TSR, are used. These techniques immediately raise the question of the degree of the polynomial. In this thesis, the polynomial is chosen based on the variance. The choice of the correct polynomial has not been further investigated in this thesis and may improve the quality of the algorithms.

In the simulation of the heat equation, there is the disadvantage that each pixel has to be simulated individually by the one-dimensional heat equation. Parallel calculation on the CPU will improve the speed of the calculation, but it is too slow to be used in the industry. Remedy, however, could be achieved in form of a calculation on the graphic card GPU, but this is associated with costs for the customer. Another remedy would be a three-dimensional simulation of the heat equation but this would go beyond the scope of this thesis. When determining the depth of the PE-HD plate, it can be observed that a maximum depth of 2mm can be determined correctly when applying the three algorithms. Drill depth, drill diameter, amount of energy and the effect of the lateral thermal diffusivity are factors that significantly affect the quality of the depth calculation.

Through this thesis, a basic theoretical understanding of the most diverse methods and areas of application of NDT is given. Furthermore, the theoretical background of light and its interaction with matter was treated. This theoretical background knowledge makes it possible to understand the principle of active thermography more precisely. The aim of this thesis was also to fulfill the flow chart of figure 8. With the presented methods and

algorithms it is now possible to fulfill this. Thus, the inhomogeneous illumination of the excitation source can now be compensated in order to increase the contrast between background and inhomogeneities and to make feature extraction methods such as PPT robust compared to inhomogeneous illumination. Through the extraction of thermal diffusivity α it is possible to simulate thermal heat equations by means of finite differences and to use them to compensate inhomogeneous excitation. Furthermore, a new method of depth calculation with the help of the heat equation was presented and compared with known methods. It is also possible through this work to go through this flow chart and the entire process. Considering the above suggestions, it is possible to improve individual components and achieve better results

In general, as already mentioned, active thermography is a powerful application technology with a lot of potential benefits and is furthermore very well accepted in the industry.

References

- [1] Camera types. <http://www.flir.de/science/display/?id=65982>. Accessed: 2017-10-29. 4, 25
- [2] Cooled or uncooled? <http://www.flir.com/science/display/?id=65982>. Accessed: 2017-12-12. 8, 24
- [3] Discrete wavelet transform filter bank implementation. <https://www.dsprelated.com/showarticle/115.php>. Accessed: 2018-01-21. 4, 37
- [4] Finding the optimum polynomial order to use for regression. <https://autarkaw.org/2008/07/05/finding-the-optimum-polynomial-order-to-use-for-regression/>. Accessed: 2017-12-12. 46, 47
- [5] Introduction to nondestructive testing. <https://www.asnt.org/MinorSiteSections/AboutASNT/Intro-to-NDT>. Accessed: 2017-12-11. 10
- [6] Irt test. <http://ars.els-cdn.com/content/image/1-s2.0-S0306261914008083-gr13.jpg>. Accessed: 2017-08-08. 4, 15
- [7] Magnetic leakage flux test. http://www.ndttechnologies.com/products/magnetic_particle_testing.html. Accessed: 2017-08-08. 4, 15
- [8] Penetrate testing. <http://www.arihantndt.com/index.php/penetrant-testing-pt>. Accessed: 2017-08-08. 4, 13
- [9] Penetrate testing. http://www.vidisco.com/ndt_solutions/ndt_info_center/ndt_x_ray_gallery. Accessed: 2017-08-08. 4, 14
- [10] Resonance inspection. <http://www.ndt.net/article/v05n01/hertlin/hertlind.htm>. Accessed: 2017-08-08. 4, 11
- [11] Spectrum light. https://en.wikipedia.org/wiki/Light#/media/File:EM_spectrum.svg. Accessed: 2017-10-26. 4, 20
- [12] Thermal detectors. <https://spie.org/samples/PM236.pdf>. Accessed: 2017-11-12. 23
- [13] Ultrasonic testing. <http://www.uni-kl.de/fileadmin/kima/pdf/Ultraschallpruefung.pdf>. Accessed: 2017-08-08. 4, 12

- [14] Visual testing. <https://www.tec-eurolab.com/eu-en/visual-test-vt.aspx>. Accessed: 2017-08-08. 4, 13
- [15] Wiens law. <http://www.mysearch.org.uk/website1/html/519.Radiation.html>. Accessed: 2018-01-21. 4, 22
- [16] William herschel and the discovery of infra-red radiation. <http://practicalphysics.org/william-herschel-and-discovery-infra-red-radiation.html>. Accessed: 2017-11-12. 19
- [17] J.C. Batsale, A. Bendada, D. Maillet. Reconstitution of a non uniform interface thermal resistance by inverse heat conduction application to infrared thermography testing. *Inverse Problems in Engineering*, vol. 6, pages 79–123, 1998. 48, 49
- [18] International Atomic Energy Agency. Non-destructive testing: A guide-book for industrial management and quality control personnel. *IAEA-TCS-9*, page 296, 1999. 9
- [19] International Atomic Energy Agency. Liquid penetrant and magnetic particle testing at level 2. *Manual for the Syllabi Contained in IAEA-TECDOC-628, Training Guidelines in Non-destructive Testing Techniques*, 2000. 12, 14
- [20] Bart Dillen Anthony A. Tanbakushi, Arjen van der Sijde. Adaptive pixel defect correction. *Proceedings Volume 5017, Sensors and Camera Systems for Scientific, Industrial, and Digital Photography Applications IV*, 05 2003. 44
- [21] Souheil Benzerrouk. Active and passive thermography for the detection of defects in green-state powdermetallic compacts. *Worcester Polytechnic Institute*, 2011. 26
- [22] Technische Universitt Berlin. Finite differenzen methode. 2003. 32, 33
- [23] Langenkamp Martin Breitenstein Otwin, Warta Wilhelm. *Lock-in Thermography*. Springer, 2001. 4, 35
- [24] Guenter Klingenberg Bryan Lawton. *Transient Temperatures in Engineering and Science*. Oxford University Pressr, 2002. 56
- [25] M. Grenier C. Ibarra-Castanedo, N. P. Avdelidis. Active thermography signal processing techniques for defect detection and characterization on composite materials. *Proc. of SPIE Vol. 7661*, 2010. 26

- [26] G.M. Carlomagno. C. Meola. Recent advances in the use of infrared thermography. *Measurement Science and Technology*, 2004. [19](#)
- [27] Thomas Westermann Claus-Dieter Munz. *Numerische Behandlung gewöhnlicher und partieller Differenzialgleichungen*. Springer, 2006. [28](#), [32](#), [52](#), [56](#), [57](#)
- [28] Jean-Marc Piau Clemente Ibarra-Castanedo, Marc Genest. Active infrared thermography techniques for the nondestructive testing of materials. *Ultrasonic and Advanced Methods for Nondestructive Testing and Material Characterization*, pages 325–348, 2003. [27](#)
- [29] Tim Jones Cynthia M. Leeman. *Recommended Practice No. SNT-TC-1A*. The American Society for Nondestructive Testin, Inc., 2016. [10](#)
- [30] M. Pilla D. A. Gonzalez, C. Ibarra-Castanedo. Automatic interpolated differentiated absolute contrast algorithm for the analysis of pulsed thermographic sequences. 2004. [50](#)
- [31] B. Venkatraman D. Sharath, M. Menaka. Defect characterization using pulsed thermography. *Journal of Nondestructive Evaluation*, pages 134 – 141, 2013. [42](#)
- [32] Dugald Seely Deborah Kennedy, Tanya Lee. A comparative review of thermography as a breast screening technique. *Integrative cancer therapies*, 2009. [26](#)
- [33] Qiwen Qiu Denvi Lau. A review of nondestructive testing approach using mechanical and electromagnetic waves. *SPIE Smart Structures and Materials*, 2016. [10](#)
- [34] Anton Erhard. Aufgaben und abgrenzung der zerstörungsfreien prfung. *DGZfP-Jahrestagung 2007 - Vortrag 1*, 2007. [10](#)
- [35] Gordon C. Everstine. Numerical solution of partial differential equations. *George Washington University*, 2010. [29](#)
- [36] International Organization for Standardization. Non-destructive testing - qualification and certification of personnel. *ISO 9712*, 4:31, 2005. [12](#)
- [37] Yan R. Gao R. X. *Wavelets - Theory and Applications for Manufacturing*. Springer, 2011. [35](#)
- [38] G. Gaussorgues. Infrared thermography. *Springer*, 1994. [20](#)

- [39] James M. Ortega Gene H. Golub. *Wissenschaftliches rechnen und differentialgleichungen (eine einführung in die numerische mathematik)*. *Heldermann Verlag*, 1992. [52](#), [55](#), [56](#)
- [40] Samira Gholizadeh. A review of non-destructive testing methods of composite materials. *Procedia Structural Integrity*, pages 50–57, 2016. [10](#), [11](#)
- [41] Jasmes Gregory. The absorption, transmission, and reflection of radiant heat by fabrics. *The British Cotton Industry Research Association*, 2008. [22](#)
- [42] Benker H. *Differentialgleichungen mit MATHCAD und MATLAB*. Springer, 2005. [28](#)
- [43] Otway TH. H. *Elliptic-Hyperbolic Partial Differential Equations A Mini-Course in Geometric and Quasilinear Methods*. Springer, 2015. [29](#)
- [44] B. Raschke H. Müller, N. Piffer. Die wärmeleitungsgleichung. *Projekt aus Partielle Differentialgleichungen*, 2004. [51](#), [52](#), [53](#), [54](#), [55](#)
- [45] H. Theodore Harcke. Screening newborns for developmental dysplasia of the hip: the role of sonography. *AJR*, pages 395–397, 1994. [10](#)
- [46] Chuck Hellier. *Handbook of Nondestructive Evaluation*. McGraw-Hill Education, 2012. [19](#)
- [47] GeorgesCrabus HenriqueCoelhoFernandes, MarcGeorges. Comparison of active thermography techniques for the inspection and defect characterisation of carbon fiber composites. *23rd ABCM International Congress of Mechanical Engineering*, 2015. [15](#), [34](#)
- [48] I. Hertlin. *Akustische Resonanzanalyse*. Castell-Verlag, 2003. [11](#)
- [49] Klein M. Ibarra-Castanedo C., Gonzales D. Infrared image processing and data analysis. *Infrared Physicd and Technology, Vol. 46*, pages 95–83, 2004. [48](#)
- [50] FLIR Systems Inc. Thermal imaging cameras for industrial applications. *Thermal Image with MSX technology*, 2012. [19](#)
- [51] Adafruit Industries. Ir sensor. 2017. [19](#)
- [52] E. Fourgeau J. Morlet, G. Arens. *Wave propagation and sampling theory; Part I, Complex signal and scattering in multilayered mediay*. Geophysics, 1982. [35](#)

- [53] Lukasz Pieczonka Jakup Roemer, Tadeusz UHL. Laser spot thermography for crack detection in aluminum structures. *7th International Symposium on NDT in Aerospace*, 2015. [26](#)
- [54] Taher L. Aljundi John A. Lively. Fluorescent penetrant inspection probability of detection demonstrations performed for space propulsion. *Review of Quantitative Nondestructive Evaluation Vol. 22*, 2003. [13](#)
- [55] John H. Lienhard IV John H. Lienhard IV. *A Heat Transfer Textbook*. John H. Lienhard V, 2001. [31](#)
- [56] Scott Juds. *Photoelectric Sensors and Controls: Selection and Application*. CRC Pressr, 1988. [24](#)
- [57] Fry B. Kalantar-zadeh K. *Nanotechnology-Enabled Sensors*. Springer, 2008. [24](#)
- [58] Christoph Krall. Nonlinear signal processing. *Signal Processing and Speech Communication Laboratory*, 2005. [4](#), [39](#), [40](#), [45](#), [46](#)
- [59] Nanni Costa Luzi F, Mitchell M. *Thermography: current status and advances in livestock animals and in veterinary medicine*. Fondazione Iniziative Zooprofilattiche e zootecniche, 2013. [19](#)
- [60] V. Jacko M. Hain, J. Bartl. Active infrared thermography in non-destructive testing. *MEASUREMENT 2009, Proceedings of the 7th International Conference*, 2009. [41](#)
- [61] Th. Jentsch M. Kräning. Non-destructive testing and process control using x-ray methods and radioisotopes. *QNET*, pages 21–34, 1998. [14](#)
- [62] X. Maldague. *Theory and Practice of Infrared Technology for Nondestructive Testing*. 2001. [49](#)
- [63] X. Maldague. Introduction to ndt by active infrared thermography. *Material Evaluation*, 2002. [17](#), [26](#)
- [64] Xavier Maldague. Quantitative subsurface defect evaluation by pulsed phase thermography: depth retrieval with the phase. 2015. [21](#), [28](#), [34](#)
- [65] S. G. Mallat. Multifrequency channel decompositions of images and wavelet models. *IEEE Transactions on Acoustics, Speech, and Signal Processing*, vol. 37, pages 2091–2110, 1989. [36](#)

- [66] S. G. Mallat. A theory for multiresolution signal decomposition: the wavelet representation. *IEEE Transactions on Pattern Analysis and Machine Intelligence*, vol. 11, pages 674–693, 1989. [37](#)
- [67] Ralph Rotolante Markus Tarin. Ndt in composite materials with flash, transient, and lock-in thermography. *FLIR Technical Series*, 2011. [26](#), [28](#)
- [68] George A. Matzkanin. Selecting a nondestructive testing method: Visual inspection. *Spring*, pages 15–17, 2007. [12](#)
- [69] John Lester Miller. Principles of infrared technology: a practical guide to the state of the art. *John Wiley Sons, New York NY*, 2001. [19](#)
- [70] J. Morlet. *Sampling Theory and Wave Propagation*. Springer, 1983. [35](#)
- [71] Vasylyl Morozhenko. *Infrared Radiation*. InTech, 2012. [20](#), [26](#)
- [72] M. Stadthaus N. P. Migoun, A. B. Gnusin. New potentials of penetrant testing. *ECNDT*, 2006. [13](#)
- [73] Zaira P. Marioli-Riga Nicolas P. Avdelidis, Clemente Ibarra-Castanedo. A study of active thermography approaches for the non-destructive testing and evaluation of aerospace structures. *Thermosense*, 2008. [24](#)
- [74] Mohammed Omar. *Nondestructive Testing Methods and New Applications*. In Tech, 2012. [9](#)
- [75] Michael Pajkic. Normung fr die sichtprfung. *3. Fachseminar, Optische Prf- und Messverfahren, DGZfP*, 2013. [12](#)
- [76] Panasonic. Infrared array sensor grid-eye. 2017. [19](#), [24](#)
- [77] Henri Walaszek Patrick Bouteille, Gregory Legros. Comparison between induction thermography and conventional ndt methods for forged parts. *11th European Conference on Non-Destructive Testing (ECNDT 2014)*, 2014. [27](#)
- [78] Anna Runnenalm Patrik Broberg. Detection of surface cracks in welds using active thermography. *18th World Conference on Nondestructive Testing*, 2012. [17](#), [26](#), [27](#)
- [79] Michael Krning Peter Bieder, Gerd Dobmann. Current ndt research & development for npp inspections. *17th World Conference on Nondestructive Testing*, 2008. [11](#), [12](#)

- [80] James Nulton Peter Salamon, Bjarne Andresen. The mathematical structure of thermodynamics. pages 271–290, 2006. [29](#)
- [81] J. Guerediaga R. Usamentiaga, P. Venegas. Automatic detection of impact damage in carbon fiber composites using active thermography. *Infrared Physics & Technology*, pages 36–46, 2013. [15](#), [34](#)
- [82] N. Rajic. Principal component thermography for flaw contrast enhancement and flaw depth characterisation in composite structures. *Composite Structures, vol. 58*, pages 521–528, 2002. [38](#)
- [83] George Taranu Raluca Plesu, Gabriel Teodoriu. Infrared thermography applications for building investigation. *Bulletin of the Polytechnic Institute of Iasi - Construction and Architecture Section*, 2012. [26](#)
- [84] Andrs Restrepo and Humberto Loaiza-Correa. Background thermal compensation by filtering for contrast enhancement in active thermography. *Journal of Nondestructive Evaluation*, 2016. [48](#)
- [85] C. Maierhofer S. Goetschel, M. Weiser. Data enhancement for active thermography. *Konrad-Zuse-Zentrum fr Informationstechnik Berlin*, 2012. [42](#), [46](#), [58](#)
- [86] P. G. Bison S. Marinetti, E. Grinzato. Statistical analysis of ir thermographic sequences by pca. *Infrared Physics & Technology*, pages 85–91, 2004. [38](#)
- [87] E. M. Sparrow. *Radiation Heat Transfer, Augmented Edition*. CRC Press; 1 edition, 1978. [21](#), [22](#)
- [88] B. Heyrman T. Toczek, F. Hamdi. Scene-based non-uniformity correction: From algorithm to implementation on a smart camera. *Journal of Systems Architecture*, 2013. [44](#)
- [89] GE Inspection Technologies. Industrial radiography - image forming techniques. *GE Inspection Technologies*, 2008. [14](#)
- [90] Christopher C. Tsdell. *Engineering Mathematics: YouTube Workbook*. bookboon, 2016. [30](#)
- [91] Guerediaga J Usamentiaga R, Venegas P. Infrared thermography for temperature measurement and non-destructive testing. *PubMed*, 2014. [20](#)

- [92] Benedetto Troia Vittorio M. N. Passaro, Corrado de Tullio. Recent advances in integrated photonic sensors. *Biomedsearchr*, 2012. [23](#)
- [93] C. P. Butler W. J. Parker, R. J. Jenkins. Flash method of determining thermal diffusivity, heat capacity, and thermal conductivity. *Journal of Applied Physics*, pages 1679 – 1684, 1961. [42](#), [51](#)
- [94] J. Wendt. *Computational Fluid Dynamics An Introduction*. Springer, 2009. [29](#)
- [95] R. A. Youshaw. A guide for ultrasonic testing and evaluation of weld flaws. *Ultrasonic Test Guide to the Ship Structure Committee*, pages 1–12, 1970. [11](#)
- [96] Vrizlynn L. L. Thing Yu Chen. A study on the photo response non-uniformity noise pattern based image forensics in real-world applications. *Institute for Infocomm Research*, 2012. [44](#)
- [97] Ning Tao Zhi Zeng, Jing Zhou. Absolute peak slope time based thickness measurement using pulsed thermography. *Infrared Physics & Technology*, page 200 – 204, 2012. [41](#)
- [98] Ning Tao Zhi Zeng, Jing Zhou. Absolute peak slope time based thickness measurement using pulsed thermography. *Infrared Physics & Technology*, pages 200 – 204, 2012. [42](#)
- [99] Bedabrata Pain Zhimin Zhou, Sabrina E. Kemeny. A cmos active pixel image sensor with amplification and reduced fixed pattern noise. *Center for Space Microelectronics Technology*, 1995. [17](#), [44](#)